Regional Exploration and Characterisation of CO_2 Storage Prospects in the Utsira-Skade Aquifer, North Viking Graben, North Sea

C. Lloyd[1]*, M. Huuse[1], B. J. Barrett[2] and A. M. W. Newton[3]

[1]Department of Earth and Environmental Sciences, University of Manchester, Manchester, United Kingdom, [2]Equinor Research Centre, Equinor ASA, Ranheim, Norway, [3]School of Natural and Built Environment, Queen's University Belfast, Belfast, United Kingdom

Subsurface CO_2 storage is considered a key element of reducing anthropogenic emissions in virtually all scenarios compatible with limiting global warming to 1.5°C. The Utsira-Skade Aquifer (Utsira, Eir and Skade Formations), northern North Sea, has been identified as a suitable reservoir. Although the overall storage capacity of the full aquifer has been estimated based on regional data, it is lacking an integrated assessment of containment and internal heterogeneity, to identify optimal areas for injection and for calculation of site-specific storage capacities. A high-resolution, broadband 3D seismic reflection dataset, full waveform inverted velocity data and 102 exploration wells are utilised to provide a catalogue of CO_2 storage prospects in the northern Utsira-Skade Aquifer. This is achieved through: 1) definition of the aquifer's spatial limits; 2) calculation of porosity distribution; 3) assessment of the extent, geomorphology, thickness variability, and containment confidence (CC) of mudstones; and 4) mapping of closures through fill-to-spill simulations. CO_2 storage capacity was calculated for the prospects using two approaches; using the full reservoir thickness (FRT) beneath the closures and using only the thickness from the closure top to the spill point (TSP), i.e., within structural traps. Porosity ranges from 29 to 39% across the aquifer and is higher in the Utsira and Eir Fms. relative to the underlying Skade Fm. The mudstone separating the Skade and Eir/Utsira Fm. has a thickness > 50 m, and is a potential barrier for CO_2. Other intra-aquifer mudstones were mainly interpreted to act as baffles to flow. Structural traps at the top Utsira and Skade Fms. yield fifteen prospects, with criteria of > 700 m depth and FRT storage capacity of > 5 Mt CO_2. They have a combined storage capacity of 330 Mt CO_2 (FRT) or 196 Mt CO_2 (TSP). Five prospects have a positive CC score (total capacity: 54 Mt CO_2 FRT or 39 Mt CO_2 TSP). Additional storage capacity could be achieved through more detailed analysis of the seal to upgrade the CC scores, or through use of a network of the mapped closures with a fill-to-spill approach, utilising more of the aquifer.

Keywords: Utsira formation, Skade formation, CO_2 storage, reservoir characterisation, seismic analysis, CO_2 storage capacity, fill-to-spill analysis

INTRODUCTION

Carbon capture and storage (CCS) is now considered a necessity, not an option, for reaching net-zero greenhouse gas emissions by 2050 (Stark & Thompson, 2019). One of the key subsurface challenges for upscaling CO$_2$ storage is to identify, characterise and de-risk potential CO$_2$ storage sites. The North Sea is considered the most promising potential CO$_2$ storage hub for European industries due to the vast amount of geological pore space, subsurface data, knowledge and infrastructure already in place. Preliminary studies have shown that the Norwegian sector of the North Sea has up to 70 Gt storage capacity (Halland et al., 2011); much greater than the modelled 52−298 Mt CO$_2$ to be stored annually for the whole of Europe by 2050 (European Commission, 2018). Two thirds of the 70 Gt proposed storage capacity lie in deep saline

aquifers, while the other third is in depleted hydrocarbon fields (Halland et al., 2011). Detailed characterisation of saline aquifers is required to identify the most economically-viable and geologically-secure potential CO$_2$ storage sites (Ringrose et al., 2021). Such analyses should assess three elements: 1) CO$_2$ containment, through assessment of seal integrity, seal bypass systems and overburden migration paths (e.g., Lloyd et al., 2021; Wu et al., 2021); 2) CO$_2$ capacity, including identification of structural traps and reservoir heterogeneities (this study); and 3) injectivity, assessing the well design/placement, potential flow and trapping style of the CO$_2$ plume within the reservoir through dynamic modelling.

One of the most promising aquifers in the Norwegian North Sea is the Utsira-Skade Aquifer, which consists of three major Neogene clastic formations; the Skade, Eir and Utsira Formations (**Figure 1**). Disparities and inaccuracies in the
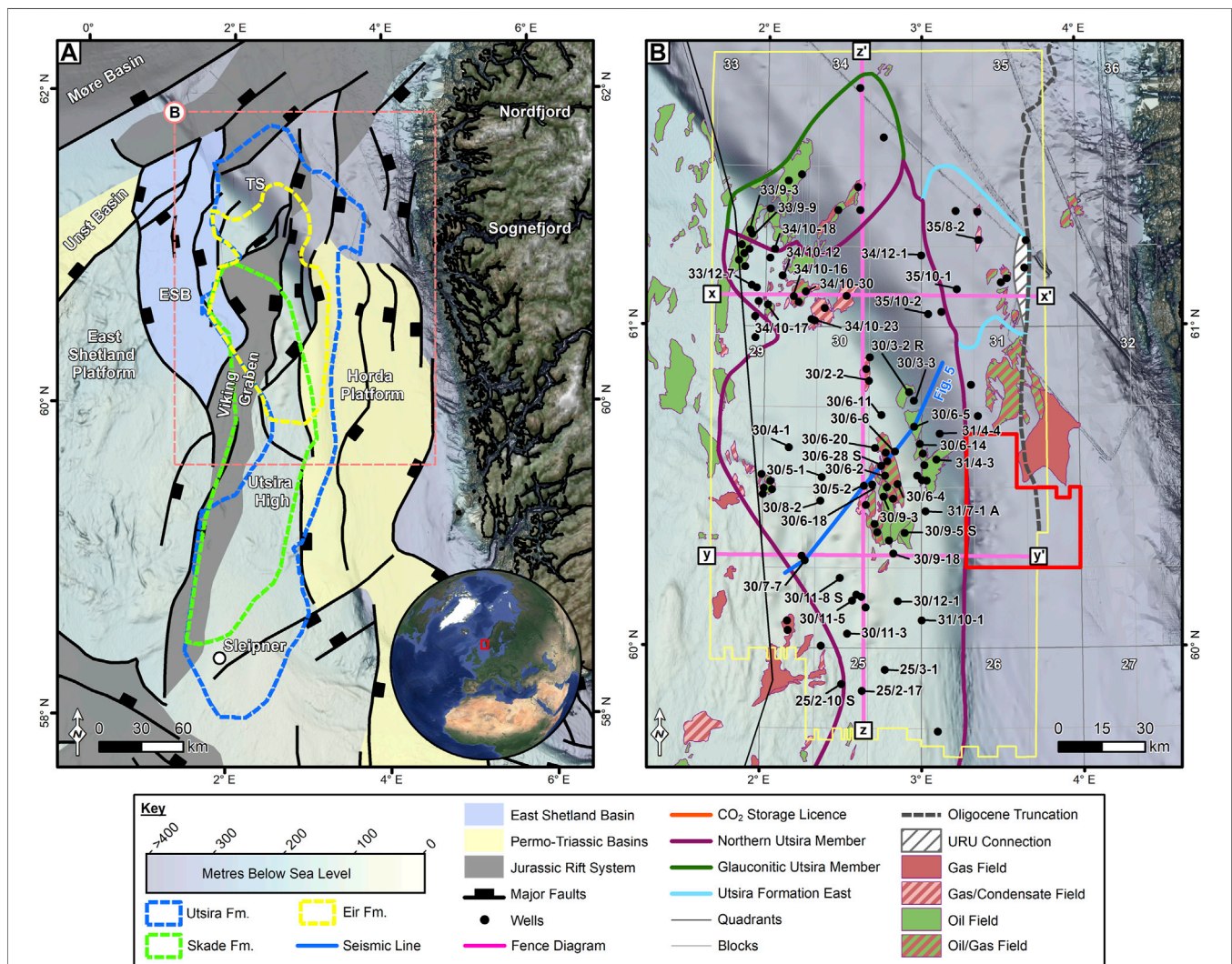

FIGURE 1 | Study area with wells and data extent. **(A)** Context of the study area in the North Sea with aquifer formation extent maps (Eidvin et al., 2013), structural elements (modified from Færseth, 1996) and the location of the Sleipner injection site. Satellite imagery from the World Imagery layer of ArcMap online. Bathymetry from EMODnet Bathymetry Consortium (2018). **(B)** Utsira Fm. outline (Eidvin et al., 2013) with seismic dataset extent (yellow) and Northern Lights CO$_2$ storage licence (red). Black dots show wells used in this study, with the named wells presented in this paper. Oil and gas fields in the region are also indicated. ESB = East Shetland Basin; TS = Tampen Spur region.
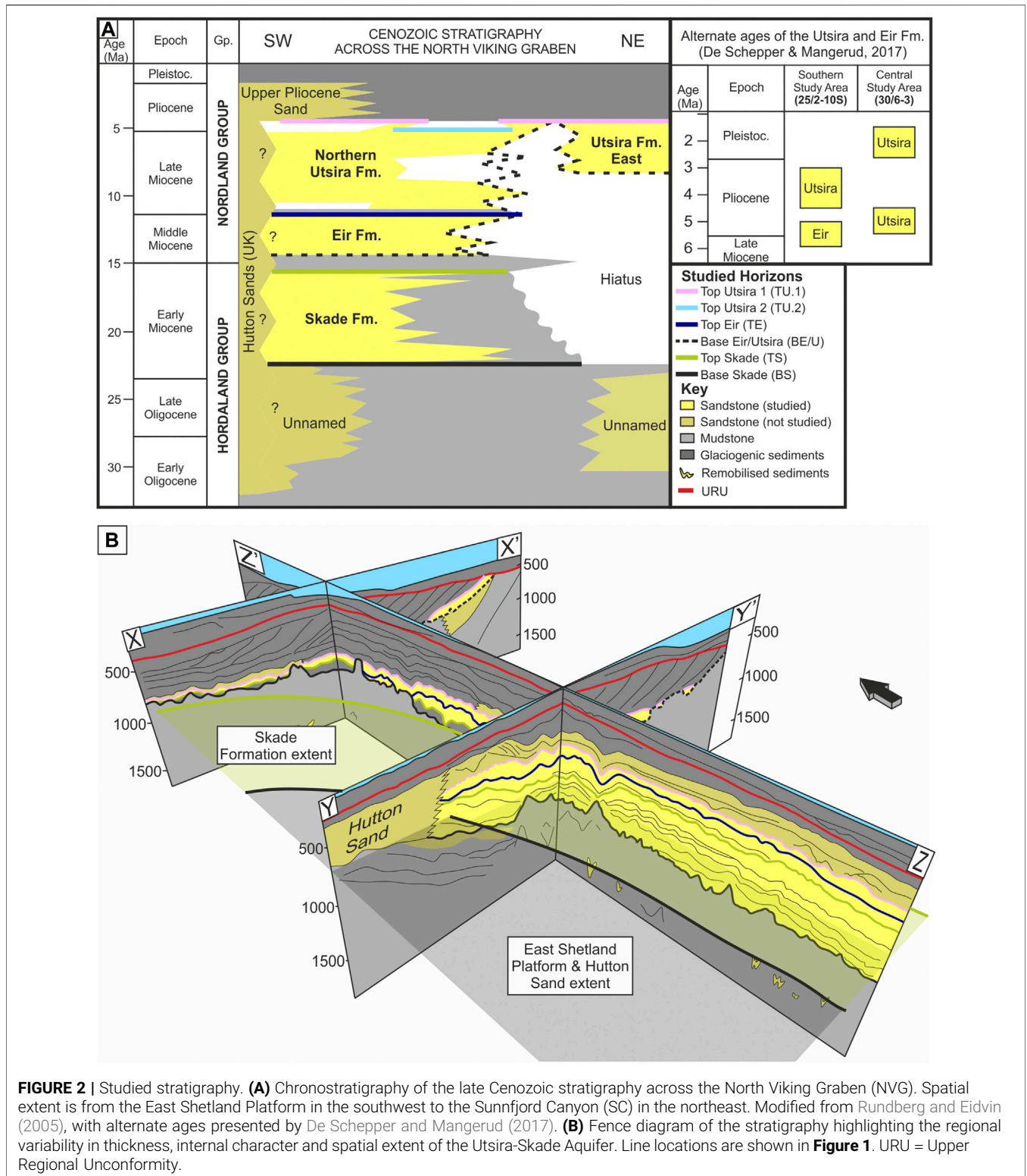
FIGURE 2 | Studied stratigraphy. **(A)** Chronostratigraphy of the late Cenozoic stratigraphy across the North Viking Graben (NVG). Spatial extent is from the East Shetland Platform in the southwest to the Sunnfjord Canyon (SC) in the northeast. Modified from Rundberg and Eidvin (2005), with alternate ages presented by De Schepper and Mangerud (2017). **(B)** Fence diagram of the stratigraphy highlighting the regional variability in thickness, internal character and spatial extent of the Utsira-Skade Aquifer. Line locations are shown in **Figure 1**. URU = Upper Regional Unconformity.

biostratigraphic analyses and age interpretations through time have led to inconsistencies in bounding definitions in well completion reports, regional seismic mapping and stratigraphic nomenclature (Eidvin et al., 2013, 2014; De Schepper & Mangerud, 2017) (**Figure 2**). There have been several attempts to quantify the CO$_2$ storage capacity of the Utsira Fm. (Holloway, 1996; Bøe et al., 2002; Chadwick et al., 2008; Lindeberg et al., 2009; Thibeau & Mucha 2011;

Gasda et al., 2017; Thibeau et al., 2018), which give a large range of capacities from 0.3 to 60 Gt CO$_2$ (Thibeau et al., 2018). Few studies have included the Skade Fm. into the capacity estimations, either as a sector model (Pham et al., 2013a), or the full Utsira-Skade Aquifer (Halland et al., 2011). The internal architecture of the aquifer, including intra-aquifer mudstones and associated closures is understudied. Such features may act as barriers that provide secure traps, or baffles that affect CO$_2$ injectivity and reduce CO$_2$ mobility in the short term. Slowed migration of CO$_2$ is desirable as it may lead to additional dissolution and geochemical trapping (Johnson et al., 2001). At the Sleipner injection site (utilising the Utsira Fm.), intra-aquifer mudstones did not slow migration to the extent that was expected, as CO$_2$ was detected at the top seal just 3 years after injection began (Cavanagh & Haszeldine, 2014). This demonstrates the importance of undertaking a thorough assessment of intra-reservoir architecture to understand potential flow dynamics.

Here, through analysis of high-quality 3D seismic reflection data, Full Waveform Inverted velocity data and 102 exploration wells, we provide a catalogue of CO$_2$ storage prospects in the Utsira-Skade Aquifer above the North Viking Graben (NVG). The objectives are to: 1) define the vertical and lateral extent of the aquifer; 2) calculate the porosity distribution across the aquifer sandstones, through application of a well data-derived function to the velocity cube; 3) identify and assess the spatial extent, geomorphology, thickness variability, and containment confidence of mudstones within the Utsira-Skade Aquifer; 4) identify structural closures within the aquifer; and 5) calculate the storage capacity of the identified prospects. We consider containment of the identified prospects through application of the containment confidence map from Lloyd et al. (2021) for the Utsira Fm. and apply the methodology to the Skade reservoir-seal pair in this study. Finally, we discuss the way forward for detailed appraisal of the prospects.

GEOLOGICAL SETTING

The structural configuration of the Norwegian sector of the North Sea basin comprises several Mesozoic structural highs and grabens. These are the result of two phases of rifting and post-rifting subsidence, in the Permo-Triassic and Late Jurassic to Early Cretaceous (Ziegler, 1990; Rundberg, 1989; Faleide et al., 2002; Fossen et al., 2010). The grabens were filled with > 2,000 m of mainly mudstone, interspersed with sandstones (Rundberg 1989; Den Hartog Jager et al., 1993; Jordt et al., 1995, 2000; Martinsen et al., 1999; Huuse & Mickelson 2004; Anell et al., 2012; Goledowski et al., 2012).

There were three major phases of sand influx into the Norwegian North Sea basin from the Oligocene to Pliocene (Eidvin et al., 2013, 2014) or Pleistocene (De Schepper & Mangerud, 2017) (**Figure 2**). The first sand influx was in the Oligocene, where gravity flows sourced from the East Shetland Platform (ESP) deposited unnamed sandstones in two regions; the southern Tampen Spur and in the Frigg Field area, which pinch out to the east (Rundberg, 1989; Rundberg & Eidvin 2005;

Gregersen & Johannessen, 2007; Eidvin et al., 2013, 2014). Meanwhile, sands sourced from the Nordfjord/Sognefjord area were deposited into the eastern part of the basin (Rundberg & Eidvin, 2005; Eidvin et al., 2013, 2014).

The second sand influx (early Miocene) was sourced from the ESP and deposited across both the North and South Viking Grabens (NVG and SVG). Sediment was transported via turbidity currents and is preserved largely as amalgamated sandstones and thin mudstones (Skade Formation, **Figures 1**, **2**) (Rundberg & Eidvin 2005; Eidvin & Rundberg 2007). Time-equivalent mudstones were deposited in the central and northern parts of the basin, beyond where the Skade Fm pinches out (Rundberg & Eidvin, 2005). Deposition of the Skade Fm. was influenced by Oligocene-Miocene mounding over large, localised areas of the NVG, caused by a combination of differential compaction, slab sliding and sand remobilisation, due to silica diagenesis and dewatering in surrounding mudstones (Løseth et al., 2003, 2013; Davies et al., 2006; Eidvin et al., 2014; Hermanrud et al., 2019). The Top Hordaland Group Unconformity (THGU) overlies the Skade Fm., representing up to 15 Ma time gap (Isaksen & Tonstad 1989; Galloway et al., 1993; Martinsen et al., 1999; Galloway, 2002; Rundberg & Eidvin 2005; Løseth et al., 2013).

The third phase of sandstone deposition was generally confined to the Middle Miocene to Pliocene (Rundberg & Eidvin, 2005; Eidvin et al., 2013, 2014), but has recently been extended to the Pleistocene (De Schepper & Mangerud, 2017) (**Figure 2**). In this phase, sandstone was first deposited in the NVG area, as a series of clinoforms prograding from the ESP, with time-equivalent mudstone deposition in the SVG. The sandstones comprise the Eir Fm. (informal) (Eidvin et al., 2013, 2014). Following this, the northern North Sea formed a narrow seaway (450 km long, 90 km wide) connecting the Møre Basin in the southern-most Norwegian Sea with the central North Sea. The strait received large volumes of sandstone in both the NVG and SVG areas, forming the Utsira Fm. (Rundberg & Eidvin 2005; Eidvin et al., 2013, 2014). Localised deposition of sandstones sourced from the Sognefjord area form a predominantly Pliocene-age sub-unit of the Utsira Fm. (Utsira Fm. East; **Figures 1**, **2**; Batchelor et al., 2017; Løseth et al., 2020). In the Tampen Spur region, the Utsira Fm. is glauconite-rich (Glauconitic Utsira Mb.; **Figure 1**; Eidvin et al., 2013; De Schepper & Mangerud, 2017). Both the Eir and Utsira Fms. comprise shelfal sands deposited by mass transport flows, separated by thin (<10 m) mudstones (Isaksen & Tonstad 1989; Rundberg 1989; Martinsen et al., 1999; Galloway 2002; Chadwick et al., 2004; Rundberg & Eidvin, 2005; Eidvin et al., 2013, 2014). These were deposited in different parts of the basin over time and the various depositional phases are interpreted to possibly correlate to global glacio-eustatic sea-level oscillations (De Schepper & Mangerud, 2017). The sandstones of the Skade, Eir and Utsira Fms. are thought to act as a single aquifer system, connected up-dip on the ESP at the transition to the time-equivalent Hutton Sands in the UK (**Figure 2**; Halland et al., 2011; Eidvin et al., 2013).

The Naust Fm. overlies the Utsira Fm. (Eidvin et al., 2013; Ottesen et al., 2014; 2018; Batchelor et al., 2017; Løseth et al.,

2020). It comprises east- and west-prograding clinoforms; fluvio-deltaic sandstones from the ESP (Upper Pliocene Sand; **Figure 2**) and mud- and occasionally sand-prone glaciomarine diamicton, as well as glaciofluvial deposits from the Norwegian margin (Ottesen et al., 2012, 2018; Eidvin et al., 2013; Batchelor et al., 2017; Løseth et al., 2020). The Naust Fm. is intersected by a regional unconformity, the Upper Regional Unconformity (URU), which removed the topsets of many of the clinoforms (Ottesen et al., 2014; Lloyd et al., 2021). Above the URU, the Naust Fm. deposition and reworking was influenced by successive late Quaternary glaciations (Stewart et al., 2013; Ottesen et al., 2014).

STUDY AREA AND DATASET

This study focuses on the northern Utsira-Skade Aquifer from 30 km south of 60°N to 62°N (**Figure 1**). Complete 3D seismic coverage of the area is achieved using the 35,400 km^2 3D BroadSeis^{TM} seismic reflection survey of the NVG, acquired, processed and provided by CGG.

The BroadSeis^{TM} seismic reflection data, originally recorded in the time-domain (two-way-travel time, TWT) have been converted to depth using advanced full-waveform inversion (FWI) that iteratively estimates the subsurface velocity field, including absorption effects caused by shallow features (Hayes et al., 2018). We use the FWI velocity cube, calibrated with wells, to estimate the sandstone porosity distribution across the aquifer (**Section 4.2**). The depth-converted seismic data have a measured dominant wavelength of ca. 20 m, providing a vertical resolution of ca. 5 m (λ/4) and limit of detectability of ca. 0.7 m (λ/30) within the studied interval. The FWI velocity cube has a vertical resolution of ca. 20 m, which is estimated from the voxel size of the cube. The sub-sampled line spacing is 37.5 m for both in- and cross-line directions, which is greater than the migrated Fresnel zone and thus is the main limitation in horizontal resolution. Seismic data are presented here with ca. 20x vertical exaggeration and as zero phase with the American polarity convention, whereby a downwards increase in acoustic impedance is represented by a positive reflection and the peak is shaded with blue.

The full-stack volume was cropped to focus on the aquifer and allow easier manipulation of the data (**Figure 1**). The stratigraphic interval of interest (Skade, Eir & Utsira Fms.) extends down to ca. 1,600 m, but deeper structural features such as the Tampen Spur (TS), NVG and the ESP are used as spatial reference points (**Figure 1**). The first CO$_2$ storage exploration licence in the Norwegian North Sea, awarded for the Northern Lights Project (Exploitation Licence 001, EL001), is located within the limits of the seismic survey and is also used as a reference point (**Figure 1**). Future upscaling of the Northern Lights Project will likely result in further licensing around the vicinity of EL001, thus increasing the viability of proximal storage sites, which warrant characterisation.

This study also benefits from open-access data (Norwegian Petroleum Directorate) from 102 exploration wells that penetrate the Utsira-Skade Aquifer. Most of the wells are clustered around prolific hydrocarbon provinces (Tampen Spur region) or plays (e.g., tilted Jurassic fault blocks). 83 of the studied wells have a full lithological column interpreted from petrophysical logs and well completion reports, provided by TGS with their Facies Map Browser (FMB) tool, which is described in Lloyd et al. (2021).
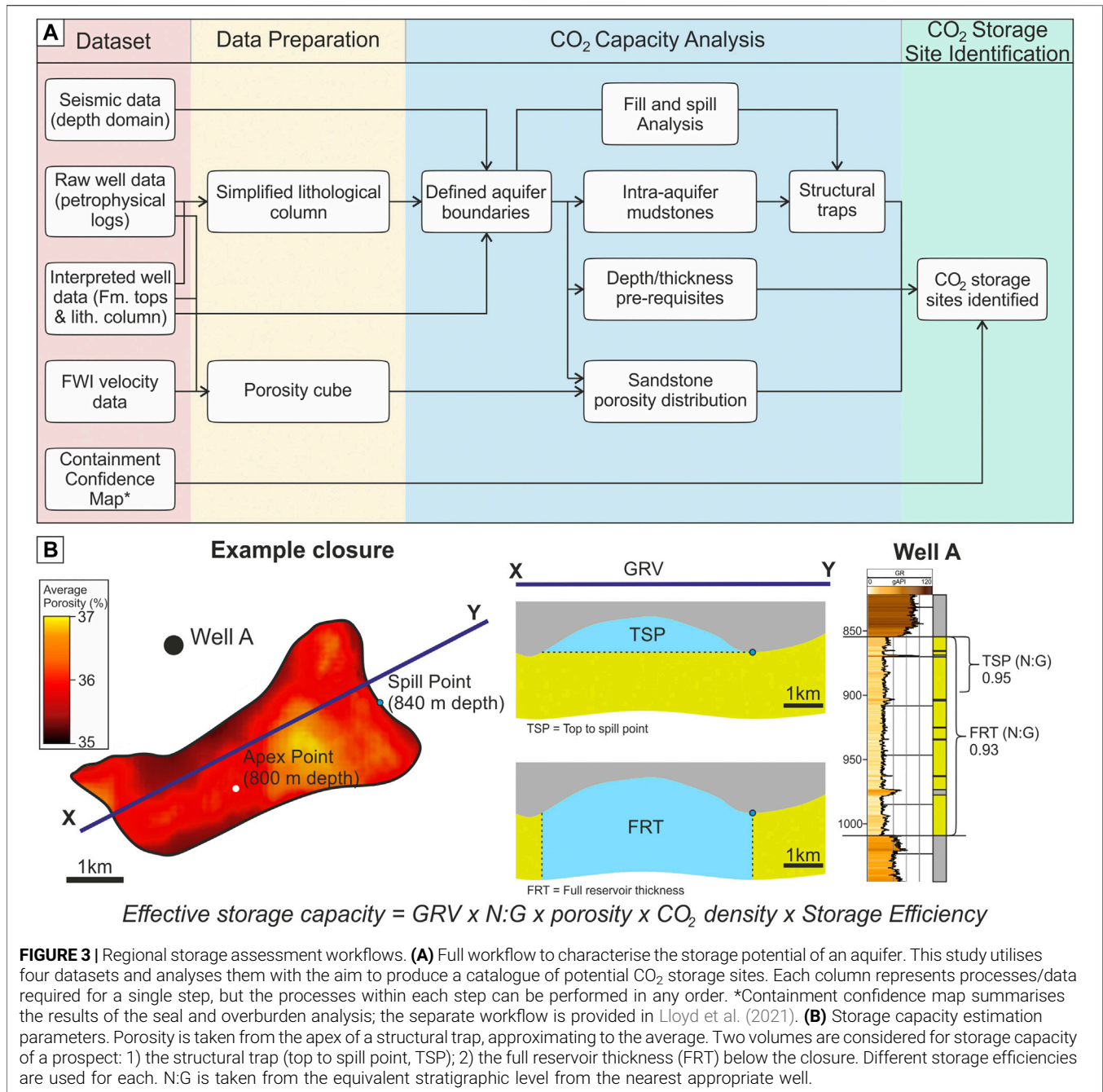
METHODOLOGY

Workflow Overview

To characterise the Utsira-Skade Aquifer for CO$_2$ storage, a workflow was adopted that could be applied to any aquifer to assess the: 1) stratigraphic boundaries of the aquifer; 2) sandstone porosity distribution; 3) intra-aquifer mudstone geometry and character; and 4) structural closures, CO$_2$ migration paths and prospect storage capacities (**Figure 3A**).

The bounding aquifer surfaces were defined using published seismic cross-sections (Eidvin & Rundberg, 2001; Rundberg & Eidvin, 2005; Gregersen & Johannessen, 2007; Eidvin et al., 2013; Løseth et al., 2013; Ottesen et al., 2014), maps (Chadwick et al., 2002; Halland et al., 2011; Eidvin et al., 2013), well formation tops (NPD), well correlations and interpretation of the seismic reflection data (Petrel^{TM} software). Some disparities in formation boundaries between publications and well reports were apparent, and in those cases, the most recent definitions of the formations are used (Halland et al., 2011; Eidvin et al., 2013).

Lithology interpretations for each exploration well were extracted from the TGS FMB tool. Lithologies were simplified into three groups ("sandstone," "mudstone" and "other") to allow for easier comparison and correlation between wells and to highlight potential reservoir (sandstone) and sealing (mudstone) stratigraphy. For example, silty sandstones and muddy sandstones are classified as "sandstones", and claystones, siltstones, and sandy siltstones are classified as "mudstones". To increase the spatial distribution of the lithology data, additional wells were manually interpreted using petrophysical logs and well completion reports. The manually interpreted wells tended to have poorer quality data, or an incomplete set of petrophysical logs in the studied interval.

Manual seismic interpretation of intra-aquifer surfaces, representing intra-reservoir mudstone layers, was augmented with semi-automated horizon tracing to interpret as many wavelets in the studied interval as possible (Paleoscan^{TM}; summarised by Daynac et al., 2016). Auto-generated interpretations were repeatedly quality-checked using cross-section validation and were modified where necessary to ensure geological accuracy. Seismic volume attributes were extracted onto the resultant surfaces to assess and highlight geological and geomorphological features. Spectral decomposition was performed using frequencies of 17 (red), 24 (blue) and 38 (green) cycles per km (c/km), which cover the frequency spectrum (GeoTeric^{TM} software).

FIGURE 3 | Regional storage assessment workflows. (A) Full workflow to characterise the storage potential of an aquifer. This study utilises four datasets and analyses them with the aim to produce a catalogue of potential CO$_2$ storage sites. Each column represents processes/data required for a single step, but the processes within each step can be performed in any order. *Containment confidence map summarises the results of the seal and overburden analysis; the separate workflow is provided in Lloyd et al. (2021). (B) Storage capacity estimation parameters. Porosity is taken from the apex of a structural trap, approximating to the average. Two volumes are considered for storage capacity of a prospect: 1) the structural trap (top to spill point, TSP); 2) the full reservoir thickness (FRT) below the closure. Different storage efficiencies are used for each. N:G is taken from the equivalent stratigraphic level from the nearest appropriate well.

Sandstone Porosity Distribution

Several studies have investigated the relationship between acoustic velocity and porosity (e.g., Eberhart-Phillips et al., 1989; Lee, 2003). Petrophysical logs and lithological interpretations were used in conjunction with the FWI seismic velocity cube to create a 3D porosity volume of the Utsira-Skade Aquifer sandstones (**Figure 4**). This approach allows for porosity estimations in areas with limited well data.

We defined a function that relates velocity to porosity of sandstones using density and sonic logs from the interval of interest. Of the 102 studied wells, only 20 contained both logs sampling the whole aquifer (**Figure 4A**), and 17 of those were usable in terms of log quality and well location. Porosity is calculated from the density logs (**Equation 1**; **Figure 4Ev**), and velocity calculated from the sonic logs (**Equation 2**; **Figure 4Evi**). Calculation of porosity using the neutron logs corresponded well with porosity from the density logs in the nine wells in which it was recorded (R = 0.97).

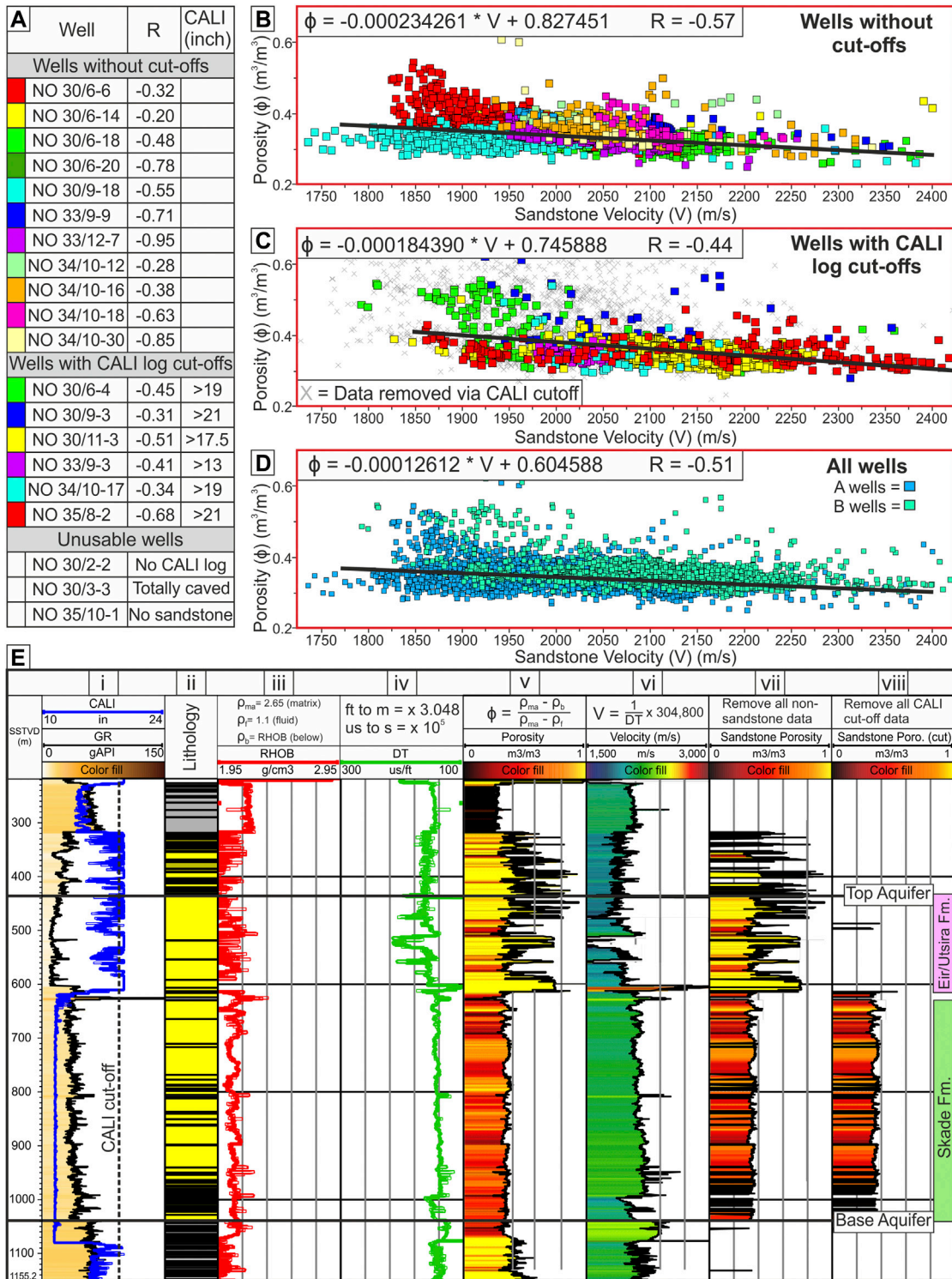$$\varnothing = \frac{\rho_{ma} - \rho_b}{\rho_{ma} - \rho_f} \qquad (1)$$

FIGURE 4 | Relationship of sandstone porosity vs sandstone velocity. **(A)** Wells used to calculate the velocity-porosity function, their correlation coefficient (R) and the required caliper cut-off. **(B)** Cross-plot of the 11 wells that did not require any modification of the data (no cut-offs). **(C)** Cross-plot of the six wells that required caliper log cut-offs due to caving. **(D)** Both sets of wells from "**(B)**" and "**(C)**" combined with a linear line of best fit. **(E)** Example log for well 30/11-3 showing the workflow (left to right). Ei = gamma ray (GR) and caliper (CALI) log, Eii = lithology log, Eiii = density (RHOB) log, Eiv = sonic (DT) log, Ev = full porosity log, Evi = velocity log, Evii = sandstone porosity log, Eviii = sandstone porosity log with caliper cut-off. The caliper log in Ei shows that the top section of the aquifer has caved in sections, resulting in porosity values that reach 70–80% (Ev), and therefore these values have been removed (Eviii). Logging was performed in a 14.75 inch pilot hole down to 625 m, and a 12.25 inch pilot hole down to 1,097 m.

where: Ø = sandstone porosity; ρ_b = formation bulk density (log value); and ρ_f = density of the fluid saturating the rock immediately surrounding the borehole (g/cm^3) – in this case saline water, 1.1 g/cm^3; ρ_{ma} = matrix density (g/cm^3) – we used 2.65 g/cm^3, which is typical for clean sandstones. We acknowledge that there are uncertainties in glauconitic areas (Rundberg & Eidvin, 2005), which could range in density from 2.40 to 2.95 g/cm^3 (Patchett et al., 1993). Since 2.65 g/cm^3 sits within this range, we deem it a suitable average across the range of sandstones present.

$$v = \frac{1}{DT} \times 304,800 \qquad (2)$$

where: v = sandstone velocity (m/s); DT = sonic log value (μsec/ft); 304,800 = multiplier for conversion from μsec/ft to m/s.

The non-sandstone datapoints were removed using the lithology column to give a well log of porosities for the sandstones (**Figure 4Evii**). The intra-formation mudstones were excluded as they are predominantly below the resolution of the velocity cube (20 m). If they are included, the well porosity values are <1% higher, and as their volumetric proportion relative to sandstones is low, their contribution to the porosity cube is minimal. For seven of the studied wells, the caliper readings were out-of-gauge through some sections, primarily indicating caving of the formation related to the low consolidation of the Utsira and Skade Fm. sandstones (**Figure 4Ei**, blue curve). This creates spurious readings in the logs, particularly the density log (ca. 1.35 g/cm^3; implying a very low density sandstone). If such data are applied to the porosity calculation (**Equation 1**), anomalously high porosity values are calculated (**Figure 4Ev**). Therefore, we used a caliper cut-off to remove all the data affected by the changing borehole size (**Figure 4Eviii**).

Sandstone porosity and velocity (ø and v) were cross-plotted on a well-by-well basis for the wells without (**Figure 4B**) and with caliper log cut-offs (**Figure 4C**), and a linear function defining the relationship between them (and a correlation coefficient) was calculated. Overall, there is a negative linear association between the two parameters, with porosity decreasing with increasing velocity (**Figures 4B–D**). The correlation coefficient (R) ranges from 0.015 to −0.84, with two wells displaying very weak to no correlation (R = 0 to −0.19), two wells showing weak correlation (R = −0.2 to −0.39), eight wells showing a moderate correlation (R = −0.4 to −0.59), four wells showing a strong correlation (R = −0.6 to −0.79) and one well showing a very strong correlation (R = −0.8 to −1) (**Figure 4A**). Hence, >75% of wells show a moderate to very strong correlation between porosity and velocity. There is a higher correlation coefficient between the wells with the applied caliper cut-off (R = −0.44, **Figure 4C**) than those without (R = −0.35, **Figure 4B**). Combining the data from all 17 wells gives the functional relationship of porosity and velocity well data (**Equation 3**), which has a moderate correlation coefficient of −0.41 (**Figure 4D**).

$$Porosity = -0.00015251 \times velocity + 0.663317 \qquad (3)$$

Equation 3 has been applied to the FWI seismic velocity cube, converting it to a porosity cube (calibrated to sandstones), which is used to assess porosity distribution across the aquifer. Any velocity artifacts in the FWI cube will be included in the porosity cube. The function shows a large range in velocity (~600 m/s) compared to porosity (~10%), which subdues small velocity changes when converting to a porosity cube. The low number of input wells, the range of correlation coefficients and the overall moderate correlation of the two variables implies uncertainty in the porosity cube.

Structural Trapping Analysis

To map structural closures and the potential migration paths from the top of each formation we used Permedia™'s fill-and-spill workflow. For this, source points are manually selected for fluid entering the system (potential CO$_2$ injection points). The up-dip fluid migration is simulated beneath a sealing surface until it is trapped in a structural closure, or it reaches the boundary of the map. Random source points (*n* = 800) were selected to highlight the potential migration routes and structural closures in each of the formations. This method only considers structural gradients to determine fill-and-spill. It does not consider physical and chemical processes that act over different timescales, and their impact on fluid migration and trapping. We used this process to highlight the 100 closures with the largest volumes at the top surface of each formation. Care was taken not to include structural closures caused by seismic artifacts. These can include velocity pull-ups, horizon mis-picks or onlaps onto underlying mounds, the latter of which are prevalent in this study. The authenticity of each individual closure was validated using seismic cross-sections.

To quantitatively assess the storage potential of the prospects, we used the equation for effective storage capacity (**Equation 4**). For each prospect, we assessed the storage capacity within the structural trap (top to the spill point of the closure, "TSP"; **Figure 3B**) and for the full reservoir thickness immediately below the closure ("FRT"; **Figure 3B**):

$$Effective\ storage\ capacity = GRV \times Porosity \times N{:}G$$
$$\times CO_2\ density \times SE \qquad (4)$$

where: GRV = Gross Rock Volume (MM Sm^3); N:G = Sandstone net-to-gross; CO$_2$ density in the reservoir = 500 kg/Sm^3 at 800 m depth (International Energy Agency, 2008; Halland et al., 2011); SE = Storage Efficiency (fraction of the reservoir pore space that can be filled by CO$_2$; Chadwick et al., 2008). Porosity was taken from the closure apex as a single value from the porosity cube for both storage capacity calculations, as there is low vertical porosity variability within each formation and it approximates to the average. N:G is taken from the equivalent stratigraphic interval in the most appropriate nearby well (**Figure 3B**). The Storage Efficiency parameter is not an intrinsic property of the reservoir, and therefore it is likely the greatest uncertainty in the capacity calculations. For the FRT, storage efficiency estimates for

aquifers (total pore volume) typically range from 2 to 8% (May et al., 2005), but can be >10% (Bachu, 2015). We use a central value of 5%, based on data from the Sleipner injection site (in 2013) (Thibeau et al., 2018). The Sleipner site does not have a distinct closure at the top of the reservoir and the full aquifer thickness is used for storage. For the TSP cases, there is a greater reliance on structural trapping due to the defined structural closure (rather than other physical and chemical trapping), and limitation of lateral migration of the plume. Therefore, a greater proportion of the GRV can be assumed to trap CO$_2$ in an open system. Natural gas storage facilities that use structural traps have (TSP) storage efficiency values that range between 3 and 40% (Larsen et al., 2007; Vangkilde-Pedersen et al., 2009). The range is high due to its dependency on properties such as trap geometry (Gorecki et al., 2009) and reservoir character (Okwen et al., 2014). We use a central SE value of 20% for TSP capacity calculations. There is high uncertainty in the SE values, but by calculating both TSP and FRT capacities, we capture a range of outcomes for storage capacity. A wider uncertainty range could be achieved through ensemble modelling.

Containment Confidence Assessment

Containment Confidence (CC) refers to the perceived confidence that CO$_2$ will remain secure and not migrate out of the reservoir, for example through seal bypass systems. CC can be mapped across a region according to elements defined in a matrix and can be considered the inverse of leakage risk. Lloyd et al. (2021) present this approach and apply it to the Utsira Fm, the results of which are used here. If it is plausible that an intra-aquifer mudstone would act as a barrier to migration, then the containment confidence of that mudstone should be evaluated. We apply the same methodology used in the CC assessment of the Utsira Fm., but adapt the matrix (Figure 14 in Lloyd et al., 2021) to only incorporate the elements important for containment to the Skade Fm. We retain the same requirements as for the Utsira Fm., such as a 50 m minimum seal thickness (Halland et al., 2011) and the same relative scoring of the main elements in the matrix (seal interval sandstones, sandstone connectivity etc), and their individual components (e.g., proven, probable and possible sandstone). As the "Overburden Interval" is incorporated into the Utsira Fm. assessment (Lloyd et al., 2021), this aspect is not required of the deeper intra-aquifer reservoirs, so the focus for CC assessment for those is on the "Seal Interval" only (overlying 50 m).

RESULTS

Utsira-Skade Aquifer Boundaries

The aquifer is bound by the Top Utsira Fm. surface (top aquifer) and the base Skade Fm. surface (base aquifer), which transitions to the base Eir and Utsira Fm. in the east (**Figures 2**, **5**). The Skade, Eir and Utsira Fms. are laterally-equivalent to the UK Hutton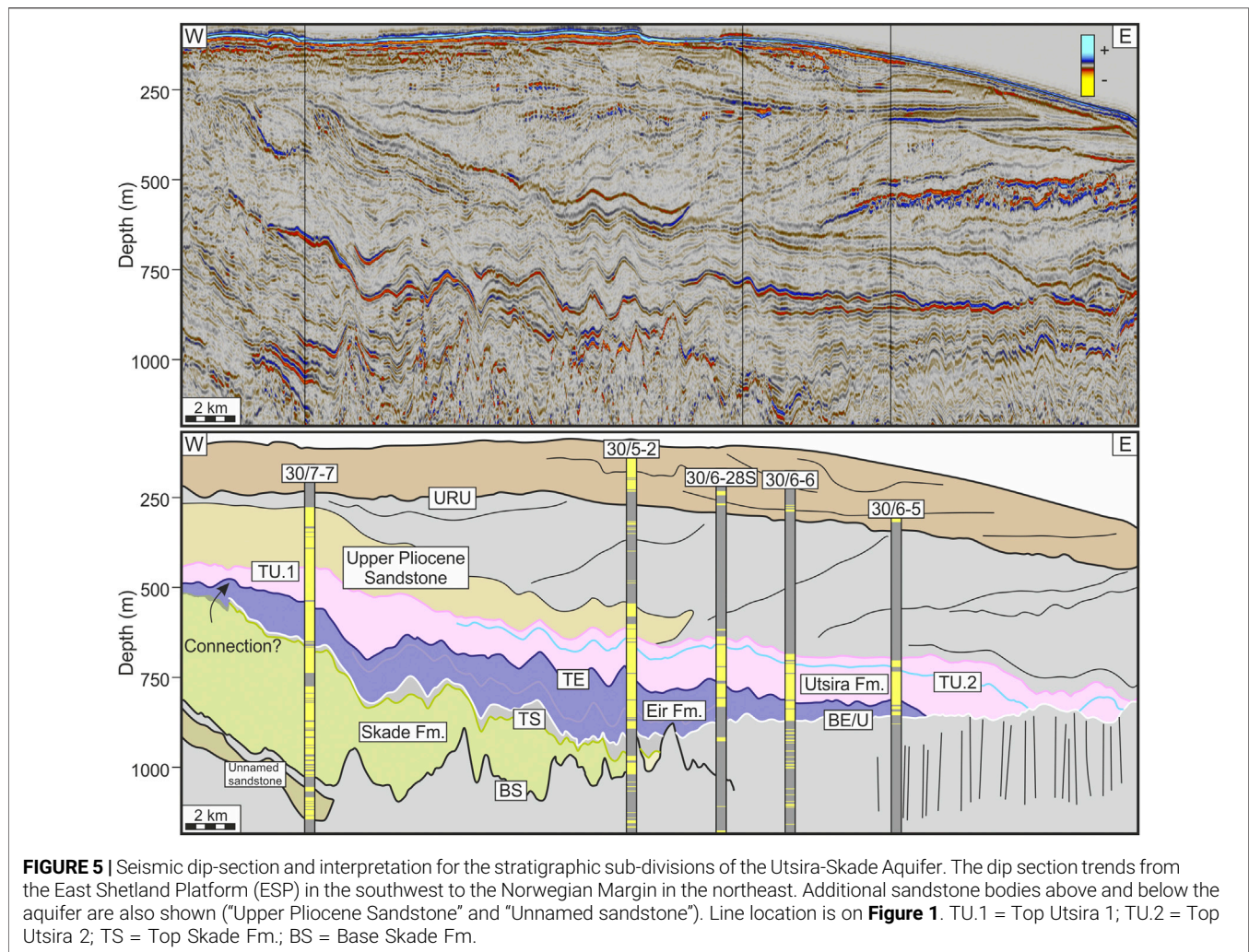 Sand in the west, on the ESP (**Figure 2**). Beneath the Skade Fm., Oligocene sandstones in the west (also part of the Hutton Sands) are interbedded and often in contact with the Skade Fm. sandstones, making it difficult to pinpoint the Skade Fm. basal boundary. Above the Utsira Fm., there are additional sandstones around the ESP and in the Tampen Spur region. These are separated from the Utsira Fm. by a mudstone of variable thickness across most of the area, however they are connected in localised areas (Lloyd et al., 2021). Underlying and overlying connected sandstones could add to the gross rock volume of the aquifer, but are omitted from our capacity analysis.

Aquifer Basal Surface

The base of the aquifer is time transgressive across the study area, formed by the base Skade Fm. in the west and the younger base Eir Fm. and base Utsira Fm. towards the east, respectively (**Figures 5, 6A**). The base Skade Fm. is deepest in the south, forming an irregular, undulating surface caused by mounding of the underlying stratigraphy (**Figure 6A**; Blocks 25/3, 30/8, 30/9, 30/11 & 30/12). These mounds are likely formed by the intrusion of underlying sand injectites, jacking-up the overlying mudstone-dominated stratigraphy at the palaeo-seafloor. In some cases, the sand intrusions may also have reached the palaeo-seafloor, depositing as extrudites (Løseth et al., 2013). Here, the stratigraphy of the Skade Fm. contains a series of sandstones with thinly bedded mudstones, which onlap and drape over the mounds (**Figure 7A**). The base Skade Fm. is sometimes difficult to follow because it is unresolved in the seismic profiles or it is not represented by a single reflection across the study area. Differentiating between extruded sandstones and basin floor fans is a challenge (Rundberg & Eidvin, 2016).

Towards the east, away from the ESP, the Skade Fm. pinches out at different stratigraphic levels, representing variable travel distances of the different clastic pulses into the basin (**Figure 7A**). Wells in this region show no major sandstones in the Skade Fm. interval (Wells in Block 30/6 and Quadrant 31). The sandstones pinch out without any clear change in seismic character, until the reflections become polygonally-faulted, likely representing a predominantly mudstone succession (Lonergan et al., 1998; Huuse et al., 2004) (**Figures 7A,B**). The transition zone between the thick sandstones of the Skade Fm. in the east and the polygonally-faulted mudstones (with minor sandstones) towards the west is termed the "Skade pinch-out zone" (**Figures 6A**, **7A**). Beyond this zone, the base Eir/Utsira Fm. becomes the base aquifer surface (**Figure 7**). The minimum thickness of the aquifer is recorded in the Skade pinch-out zone (from the base Eir Fm.), where the Skade Fm. is characterised by thin sandstone beds with thick intervening mudstones (**Figure 7A**).

The base Skade Fm. in the area north of Block 30/4 is 200−300 m shallower than its southern counterpart (**Figure 6A**). Here, the full stratigraphic thickness of the Skade Fm. onlaps the southern side of the mounds (>50 m tall) in the area (**Figure 7B**). It is unproven whether the Skade Fm. is present on the northern side of the mounds, as there are no wells that penetrate this stratigraphy, but this area is considered part of

FIGURE 5 | Seismic dip-section and interpretation for the stratigraphic sub-divisions of the Utsira-Skade Aquifer. The dip section trends from the East Shetland Platform (ESP) in the southwest to the Norwegian Margin in the northeast. Additional sandstone bodies above and below the aquifer are also shown ("Upper Pliocene Sandstone" and "Unnamed sandstone"). Line location is on **Figure 1**. TU.1 = Top Utsira 1; TU.2 = Top Utsira 2; TS = Top Skade Fm.; BS = Base Skade Fm.
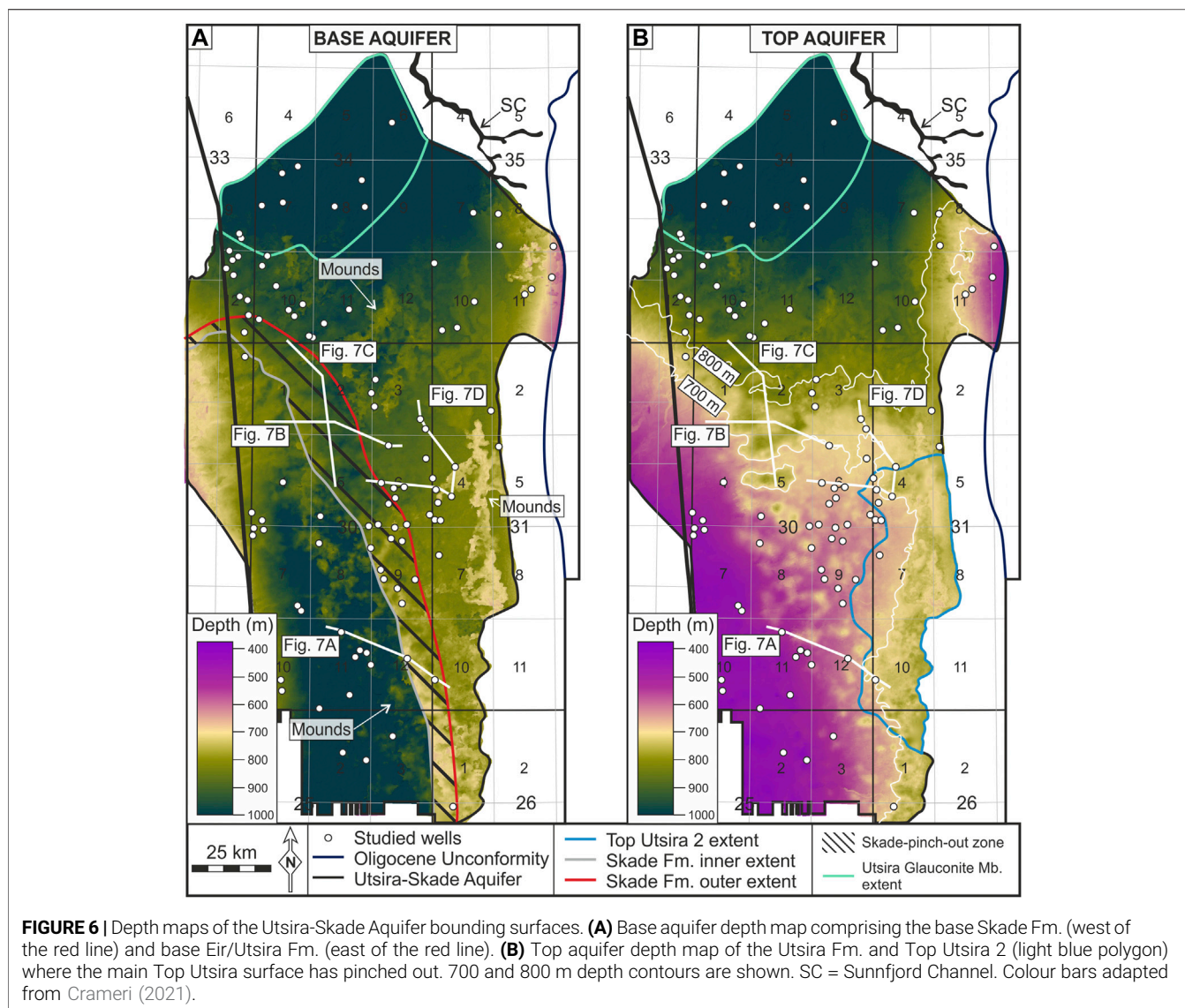
the Skade pinch-out zone based on the seismic response. The high amplitude soft response at the Skade Fm. top with low amplitude internal reflections are observed similarly to the western mound margin, and therefore sandstones could be inferred in this area (**Figure 7B**). The seismic response changes to moderate amplitude reflections further eastwards into the basin, which represents mudstone-dominated stratigraphy, proven by the nearby well (well NO 30/6-11; **Figure 7B**). In the depressions between the mounds, the Skade Fm. reflections can be traced and appear to extend further east into the basin within the Skade pinch-out zone (**Figures 6A, 7B,C**).

Where the base Utsira Fm. forms the base aquifer, the boundary with the underlying strata is mostly represented by a high amplitude, hard, continuous reflection, which represents the downwards transition from sandstone to mudstone (**Figure 7**). However, in some places interbedded sandstones make the basal reflection more challenging to pick (e.g., well NO 30/6-11, **Figure 7B**). This laterally extensive, relatively flat surface is disturbed by mounds (formed due to underlying sand intrusions) at the eastern margin (**Figure 6A**; Blocks 31/1, 31/4 & 31/7) and in the north (**Figure 6A**; Blocks 34/12 and 35/10). The

mounds are clustered, with the Utsira Fm. seismic reflections dipping down onto and onlapping the mounds (**Figures 7B,D**). The mounds on the eastern margin (**Figure 6A**; Blocks 31/4 & 31/7) are elongated and trend north-south. Wells NO 31/1-1 and NO 31/5-6 show sandstone to the east of the mounds demonstrating the aquifer extending to these regions. There is no well data available to test whether these sandstones continue south into Block 31/8, but the high amplitude, soft seismic response at the top and high amplitude, hard response at the base, with lower amplitude internal reflections is comparable to that of the main Utsira Fm. on the western margin of the mounds, suggesting that the sandstones continue into this area.

Aquifer Top Surface
The Utsira Fm. overlies both the Skade and Eir Fms. across the aquifer and therefore the Top Utsira Fm. represents the top of the aquifer (**Figure 6B**). The presence of overlying sandstone bodies above the aquifer, especially at the break of slope on the ESP (the Upper Pliocene Sandstone; **Figure 5**) and in the Tampen Spur region, have resulted in variable Top Utsira Fm.

FIGURE 6 | Depth maps of the Utsira-Skade Aquifer bounding surfaces. **(A)** Base aquifer depth map comprising the base Skade Fm. (west of the red line) and base Eir/Utsira Fm. (east of the red line). **(B)** Top aquifer depth map of the Utsira Fm. and Top Utsira 2 (light blue polygon) where the main Top Utsira surface has pinched out. 700 and 800 m depth contours are shown. SC = Sunnfjord Channel. Colour bars adapted from Crameri (2021).
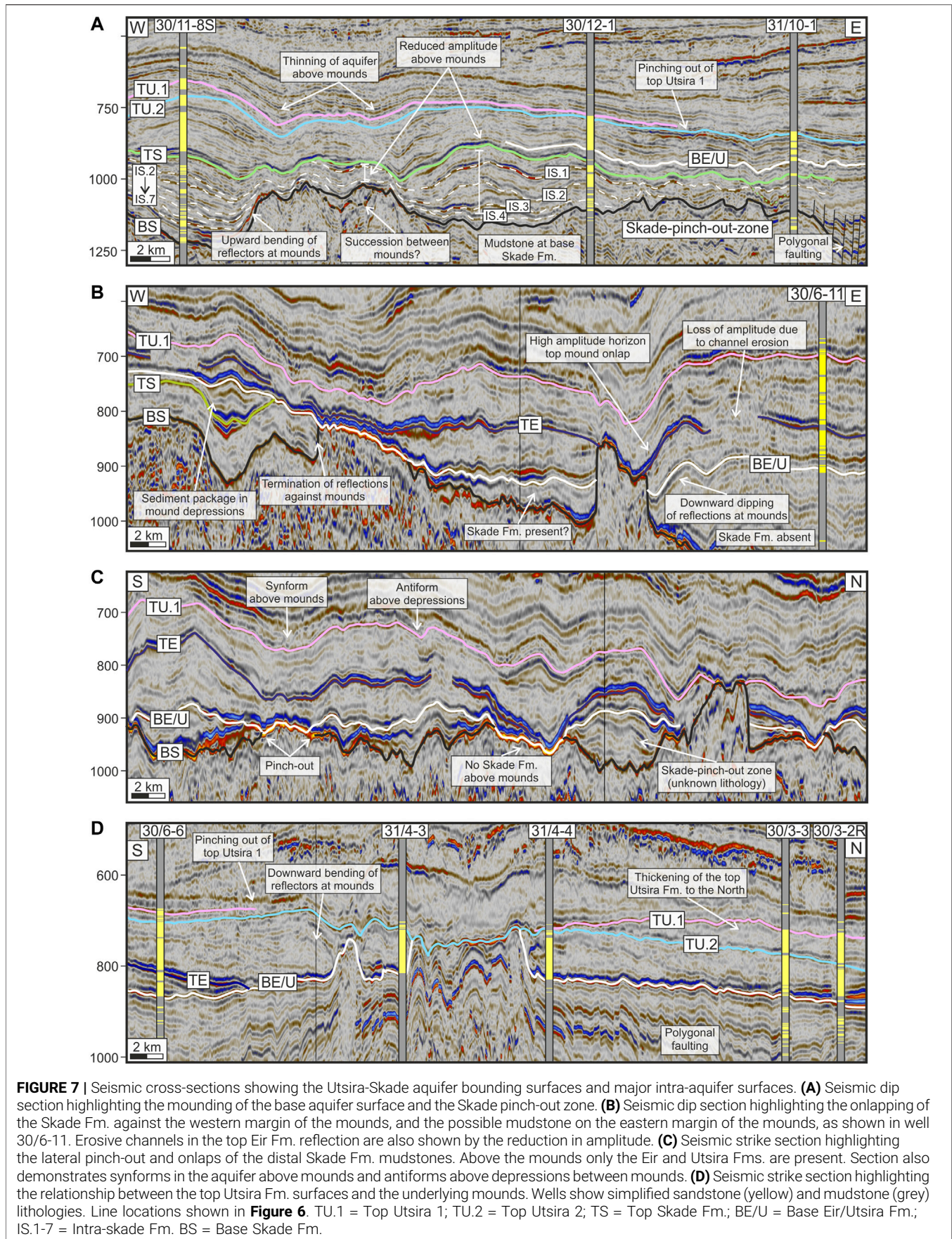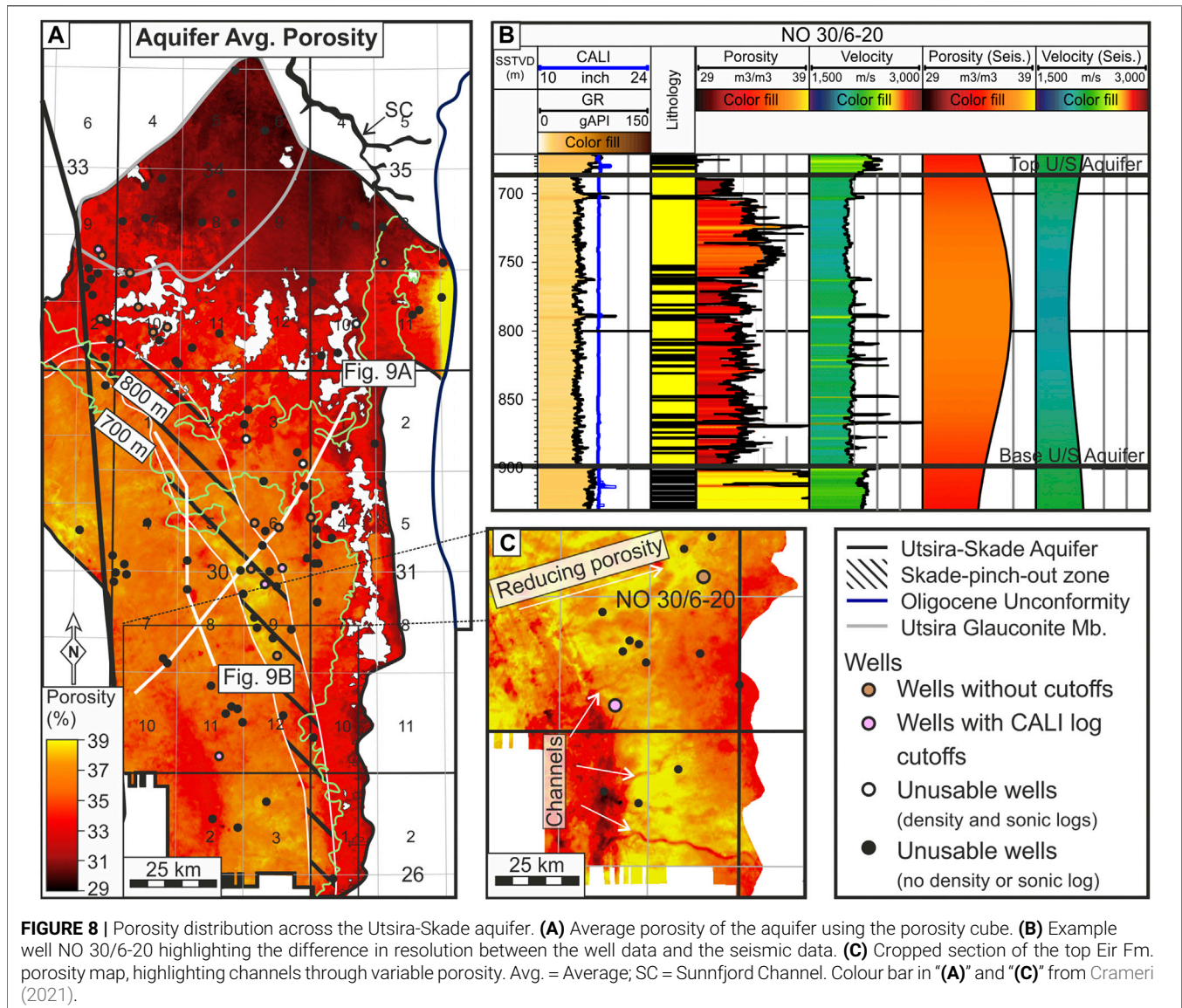
definitions in well completion reports and publications (Gregersen & Johannessen, 2007; Eidvin, 2009; Eidvin et al., 2013). The top aquifer/Utsira Fm. bounding reflection is thus not continuous across the study area, as it is characterised by a series of submarine fans with low topographic relief. The challenge with the surface pick is particularly clear in the centre of the study area (Blocks 31/4, 31/7 & 31/10), where the reflection that represents the top of the aquifer in the west, pinches out towards the east (**Figures 7A,D**). Here, the top aquifer surface drops to the underlying soft reflection (Top Utsira 2, TU.2; **Figures 6B, 7A**), which represents the top of the sandstone. This reflection (TU.2) is an intra-aquifer surface in the west. Localised depressions in the top aquifer surface often correspond to underlying mound crests of the Oligocene strata (**Figures 7A,B**). Where the top aquifer surface onlaps the mounds (in the east and north), individual reflections maintain their depositional dip until they approach a

mound, where they dip downwards towards the mound (**Figures 7B,D**).

Porosity Distribution

The well data-derived function for the sandstone porosity vs. velocity relationship (**Equation 3**, **Section 4.2**) was applied to the FWI seismic velocity cube to assess the distribution of sandstone porosity across the aquifer (**Figure 8**). The large difference in vertical resolution between the well log data (<1 m) and the FWI velocity cube (~20 m), results in a loss of the finer detail available from the wells across the 3D space (**Figure 8B**). Across the aquifer, the average porosity was calculated and is mapped on **Figure 8A**, varying from 29 to 39%. The average porosity is highest towards the south and west, and generally decreases north- and eastwards from the ESP to the northern limit of the aquifer (**Figure 9A**). The lower porosities (~29%) in the northern part of the aquifer (Blocks 34/9 & 34/12) may be the result of the distal position of the
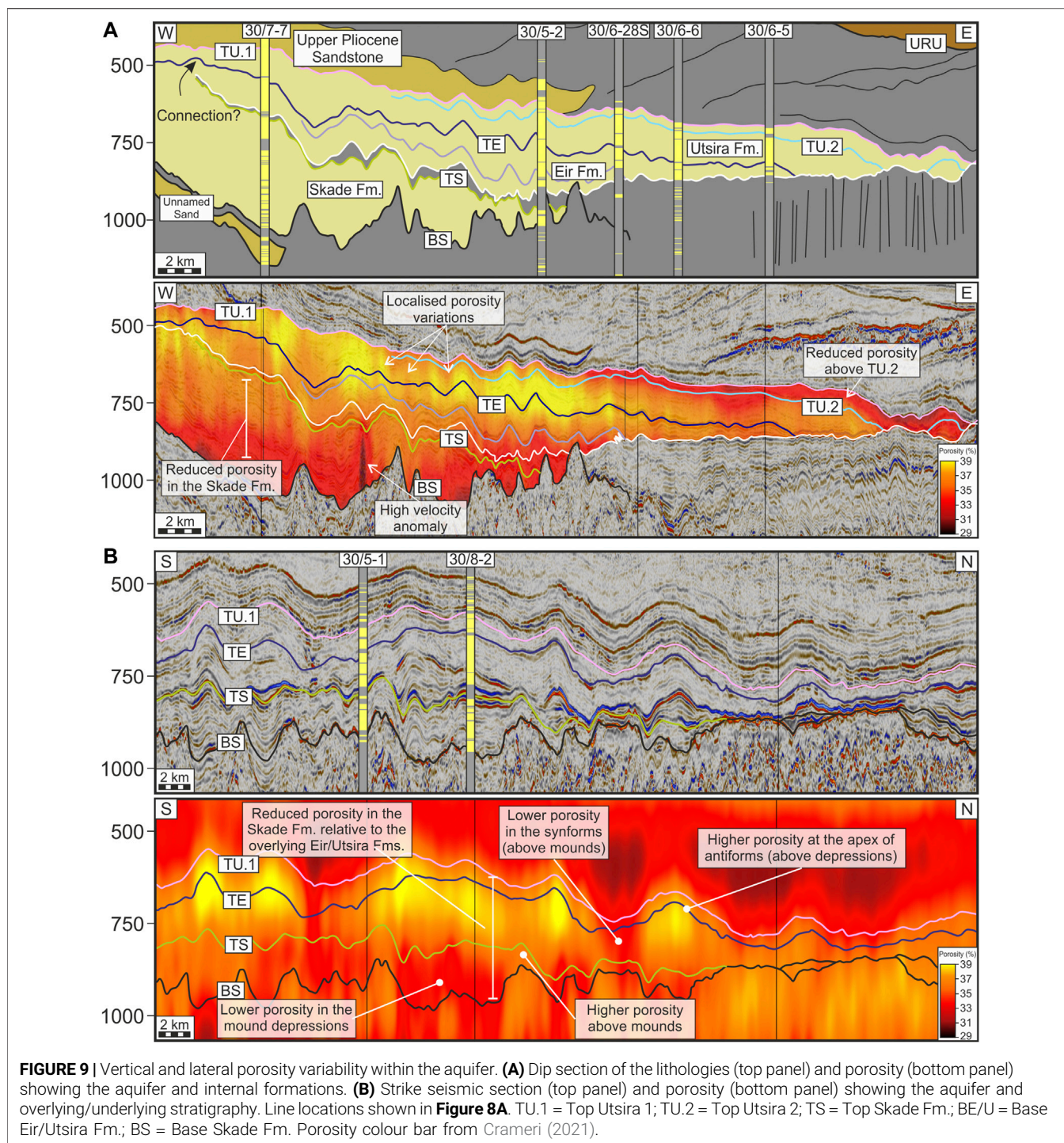
FIGURE 7 | Seismic cross-sections showing the Utsira-Skade aquifer bounding surfaces and major intra-aquifer surfaces. **(A)** Seismic dip section highlighting the mounding of the base aquifer surface and the Skade pinch-out zone. **(B)** Seismic dip section highlighting the onlapping of the Skade Fm. against the western margin of the mounds, and the possible mudstone on the eastern margin of the mounds, as shown in well 30/6-11. Erosive channels in the top Eir Fm. reflection are also shown by the reduction in amplitude. **(C)** Seismic strike section highlighting the lateral pinch-out and onlaps of the distal Skade Fm. mudstones. Above the mounds only the Eir and Utsira Fms. are present. Section also demonstrates synforms in the aquifer above mounds and antiforms above depressions between mounds. **(D)** Seismic strike section highlighting the relationship between the top Utsira Fm. surfaces and the underlying mounds. Wells show simplified sandstone (yellow) and mudstone (grey) lithologies. Line locations shown in **Figure 6**. TU.1 = Top Utsira 1; TU.2 = Top Utsira 2; TS = Top Skade Fm.; BE/U = Base Eir/Utsira Fm.; IS.1-7 = Intra-skade Fm. BS = Base Skade Fm.

FIGURE 8 | Porosity distribution across the Utsira-Skade aquifer. **(A)** Average porosity of the aquifer using the porosity cube. **(B)** Example well NO 30/6-20 highlighting the difference in resolution between the well data and the seismic data. **(C)** Cropped section of the top Eir Fm. porosity map, highlighting channels through variable porosity. Avg. = Average; SC = Sunnfjord Channel. Colour bar in "**(A)**" and "**(C)**" from Crameri (2021).

sandstones relative to the ESP sediment source, the deeper burial depth in this region, or porosity "bleeds" from the surrounding mudstones due to the low aquifer thickness (~50 m) and low resolution (~20 m). There are high porosities in the northeast in the "Utsira Formation East," as the sediments are proximal to the Sognefjord source, rather than the ESP.

Porosity of the Utsira/Eir Fm. (~37%) is higher than that of the underlying Skade Fm. (~33%) (**Figure 9A**). The Utsira Fm. at the Sleipner CO$_2$ injection site has an average porosity of 35–36% (Zweigel et al., 2004; Singh et al., 2010), and modelled values of the Skade Fm. are averaged at 32% (Pham et al., 2013a); both within 1% of our calculated porosity values. The Utsira Fm between TU.1 and TU.2 has reduced porosity (34%) relative to the rest of the Utsira Fm (**Figure 9A**). There is a localised low porosity region in the south (Blocks 30/11 & 25/2), where average porosity drops by

2–3% around the ESP relative to the surrounding aquifer (**Figures 9A**, **10A**). This is because the Utsira Fm. thins in this region (connecting to the ESP Upper Pliocene sands), resulting in greater influence from the lower porosity Skade Fm. on the average (**Figure 9A**).

Porosities from the cube were also extracted onto different intra-aquifer surfaces to assess lateral changes in porosity within individual layers (**Figure 8C**). Individual features are highlighted due to their different porosity to the surrounding area. These include pipe structures (**Figure 9A**) and channels (**Figure 8C**). These features are associated with high velocities, and thus produce low porosities through the calculation. Channels and their associated porosity changes are most apparent in the regions proximal to the sediment source, where the greatest range of grain size is assumed (**Figure 8C**).

Across-strike porosity variation is observed in the mounded areas (**Figure 9B**). In the Eir and Utsira Fms., porosities are

FIGURE 9 | Vertical and lateral porosity variability within the aquifer. **(A)** Dip section of the lithologies (top panel) and porosity (bottom panel) showing the aquifer and internal formations. **(B)** Strike seismic section (top panel) and porosity (bottom panel) showing the aquifer and overlying/underlying stratigraphy. Line locations shown in **Figure 8A**. TU.1 = Top Utsira 1; TU.2 = Top Utsira 2; TS = Top Skade Fm.; BE/U = Base Eir/Utsira Fm.; BS = Base Skade Fm. Porosity colour bar from Crameri (2021).

highest in the centre of the antiforms (above depressions between mounds), reaching up to 39% porosity. This reduces along the antiform limbs to 37%, and drops in the synforms (above mounds) to 33–34% porosity (**Figure 9B**). In the Skade Fm., a less clear trend is observed, but porosities appear to be lower in the depressions between mounds (directly below the Eir/Utsira Fm. antiforms) and higher (<37%) above the mounds (directly below the Eir/Utsira synforms)

(**Figure 9B**). We can only speculate on the cause of this porosity trend and the inverse relationship between the formations. The decreasing porosity trend in the depressions could be a depositional lithology effect whereby submarine systems routed around pre-existing or evolving mounds, preferentially depositing sand (lower porosity) in the depressions, whilst hemipelagic mud (higher porosity) accumulated at the mound tops. The mudstones are above
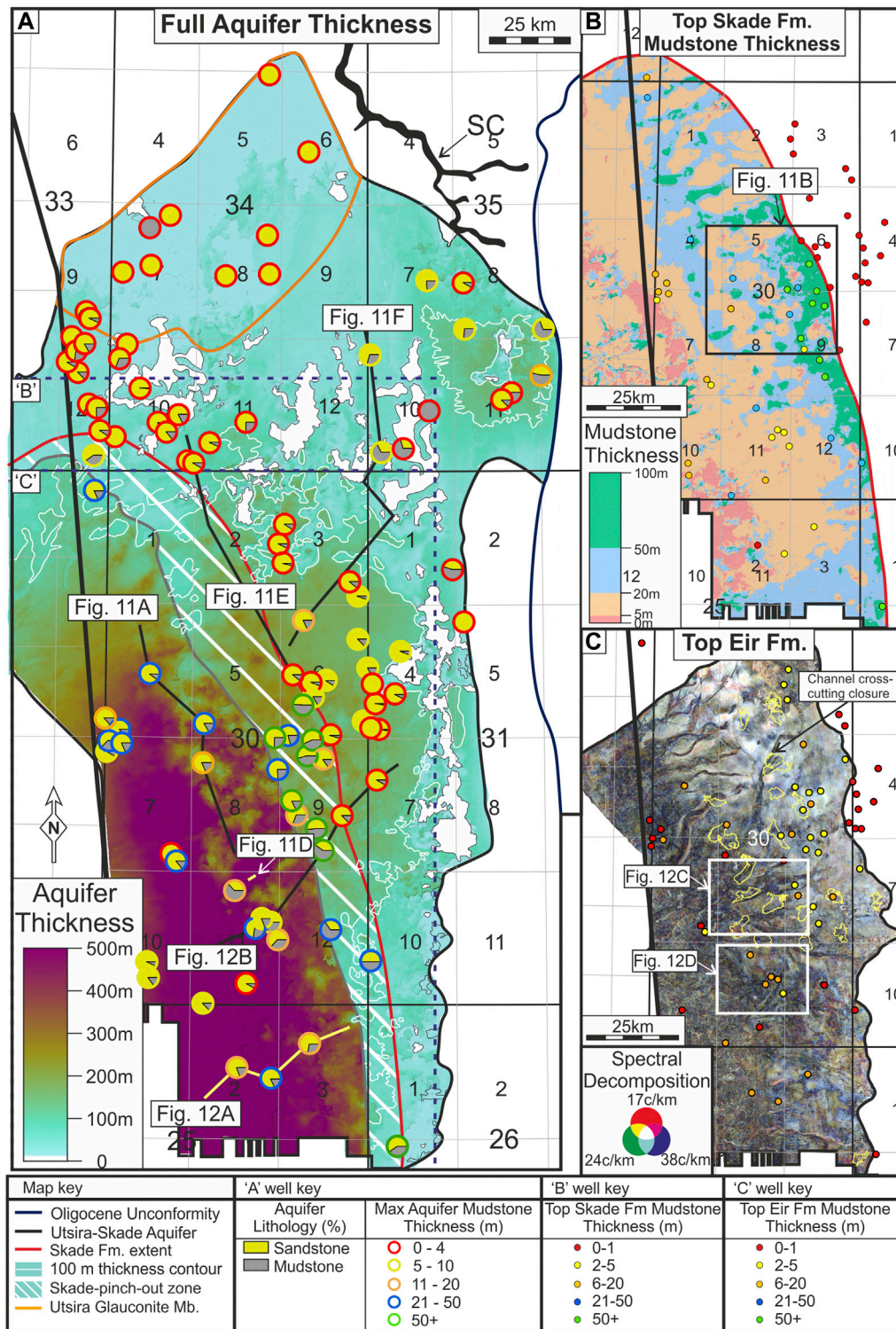
FIGURE 10 | Intra-aquifer mudstone distribution. **(A)** Aquifer net-to-gross (pie charts) and thickest mudstones (pie chart coloured perimeter) from well data, overlain onto the aquifer thickness map. The asymmetrical white shapes are where the aquifer thickness is below seismic resolution, either due to the reservoir being thin or absent, often associated with mounding. Colour bar from Crameri (2021). **(B)** Top Skade Fm. mudstone thickness in wells (well colour indicates thickness from logs) overlain onto the top Skade Fm. mudstone thickness map. **(C)** Top Eir Fm. mudstone thickness from well logs (well colour indicates thickness) overlain onto a spectral decomposition extraction from the top Eir Fm. map. The map highlights the yellow asymmetrical shapes representing the Top Eir Fm. closures that are cut by erosive channels.

the opal A/CT diagenetic transition and so preserve their high porosities (Wrona et al., 2017). The inverse porosity relationship in the Utsira Fm. is more difficult to explain since it is generally more homogenous lithologically, but could be related to compaction. Lateral compaction due to mass movements of the Hordaland (Hermanrud et al., 2019) may also have affected the porosity and warrants further study.

Intra-Aquifer Mudstones

Intra-aquifer impermeable layers, in the form of mudstones (or cemented sandstones), may affect the injectivity of a storage site through unexpected overpressure, and/or the migration and trapping of the CO$_2$ plume. Here, we focus on the extent and thickness variability of the mudstones in the Utsira-Skade Aquifer, which have been identified from well data (**Figure 10**). Several seismically-resolvable and laterally-continuous mudstone layers have been mapped across the three formations (**Figures 11**, **12**). A containment confidence assessment is performed to any mudstones that could seal CO$_2$.

Aquifer Thickness Variability and Formation-Bounding Mudstones

Considering the aquifer as a single unit, we identified the thickest intra-aquifer mudstone in each well, calculated the sandstone net-to-gross within the aquifer in that well, and overlaid the data onto a thickness map of the aquifer (**Figure 10A**). The aquifer is thickest in the central and southern regions where both Utsira and Skade Fms. are present, reaching > 500 m thickness. The thickest mudstones (50–80 m) and lowest aquifer sandstone net-to-gross are identified in the central Skade pinch-out zone (**Figure 10A**). The Skade Fm. in this zone is thin and overlain by a thick mudstone related to distal turbidite or pelagic/hemipelagic deposition. The top and base (base is the Top Skade Fm.) of this mudstone can be mapped across most of the Skade Fm., allowing a thickness map of the mudstone to be created, which corresponds well with the thickness data from wells (**Figure 10B**). To the west of the Skade pinch-out zone, this mudstone is < 50 m thick. In this central region of the Skade Fm., the mudstone is represented in areas by a single high amplitude reflection, and in others by a series of mostly high amplitude reflections (**Figure 11A**). This corresponds with the mounding of the underlying stratigraphy, where the Top Skade Fm. mudstones are thickest in the depressions, and thinnest above the mounds (**Figure 10B**). The seismic expression in the depressions is typically low amplitude homogenous reflectivity if it is mudstone, or a series of medium to high amplitude reflections reflecting interbedded mudstones and sandstones (**Figure 11A**). On the ESP, the Top Skade Fm. mudstone, represented by a single high amplitude seismic reflection, has been eroded in areas due to large canyons (**Figures 5**, **10B**). The erosion caused by these canyons likely connect the Skade to Eir and Utsira Fms. sandstones (**Figure 12A**). In the central Skade pinch-out-zone, faults are observed above the mound crests extending through the whole Top Skade Fm. mudstone (**Figures 11B,C**). In the proximal area, there are only a few faults that extend

through the Skade Fm., as the mounds are deeper and in some cases these also offset the Top Skade Fm. mudstones (**Figure 11D**). The Top Skade Fm. mudstone reaches > 50 m thick in areas of the Skade pinch-out zone, which is greater than the minimum advised seal thickness for CO$_2$ storage (Halland et al., 2011). Therefore, although connected to the Eir and Utsira Fms. up-dip to form the aquifer, the Skade Fm. can be considered as a separate reservoir for CO$_2$ storage, and requires a full containment confidence (CC) assessment (**Section 5.3.3**).

Beyond the Skade pinch-out zone, the aquifer is thickest in the central region (Blocks 30/6, 9 & 31/4, 31/7), and thins towards the north, east and south (**Figure 10A**). The aquifer is absent above the mounds, or the thickness is reduced to < 5 m (**Figure 10A**; white areas). The thickest mudstone recorded in this region is the Top Eir Fm. mudstone, which is < 10 m in wells (except NO 30/6-11, where it is 13 m; **Figure 10A**) and can be correlated across much of the central and southern aquifer (**Figure 10C**). The mudstone is thinnest where the Top Eir Fm. is at shallower depths, primarily in the south and close to the ESP. Extracting a frequency decomposition attribute onto this surface highlights multiple slope channels that appear to be amalgamated and erode the mudstone in the proximal area to the ESP (**Figure 10C**). The channels become less frequent and more isolated in the more distal regions. The northern and southern areas of the Top Eir Fm. mudstone are contrasting in terms of seismic character (**Figure 10C**). In the north, the high amplitude seismic reflection that represents the channel-cut mudstone layer sharply becomes lower amplitude, and shows a negligible impedance contrast with the overlying and underlying sandstones (**Figure 11E**). This suggests that these channels could be sand-filled. Towards the south, the channel-cut mudstone reflection maintains its high amplitude and acoustic impedance contrast, suggesting the channels in this area are mudstone-filled. This is supported by the lower frequency content of the southern channels relative to those in the north and the contrasting porosities highlighted in these channels (**Figure 8C**; although the porosity cube is not calibrated for mudstones). The thickness of the Top Eir Fm. mudstone, with a maximum thickness of 13 m from well data, is much lower than the minimum advised seal thickness for CO$_2$ storage in the North Sea (Halland et al., 2011). Therefore, this mudstone is not considered an appropriate seal for CO$_2$ storage and a CC matrix is not applied.

Intra-Formation Mudstones

In the Eir and Utsira Fms., mudstones are typically thin (<5 m), infrequent (typically 1–3 beds observed in each well), and owing to their thickness and low acoustic impedance contrast with surroundings, are not characterised by a substantial seismic amplitude response (**Figures 11A**, **12B**). In the Skade Fm., mudstones are generally thicker and produce a more defined seismic response, allowing correlation between wells (Intra-Skade (IS) 1–7; **Figures 12A,B**). The Liatårnet oil discovery is beneath the thickest and deepest intra-Skade Fm. mudstone (~20 m; NO 25/2-10S).

Spectral decomposition was performed on each of the intra-Skade mudstone surfaces (IS. 1–7) to highlight cross-
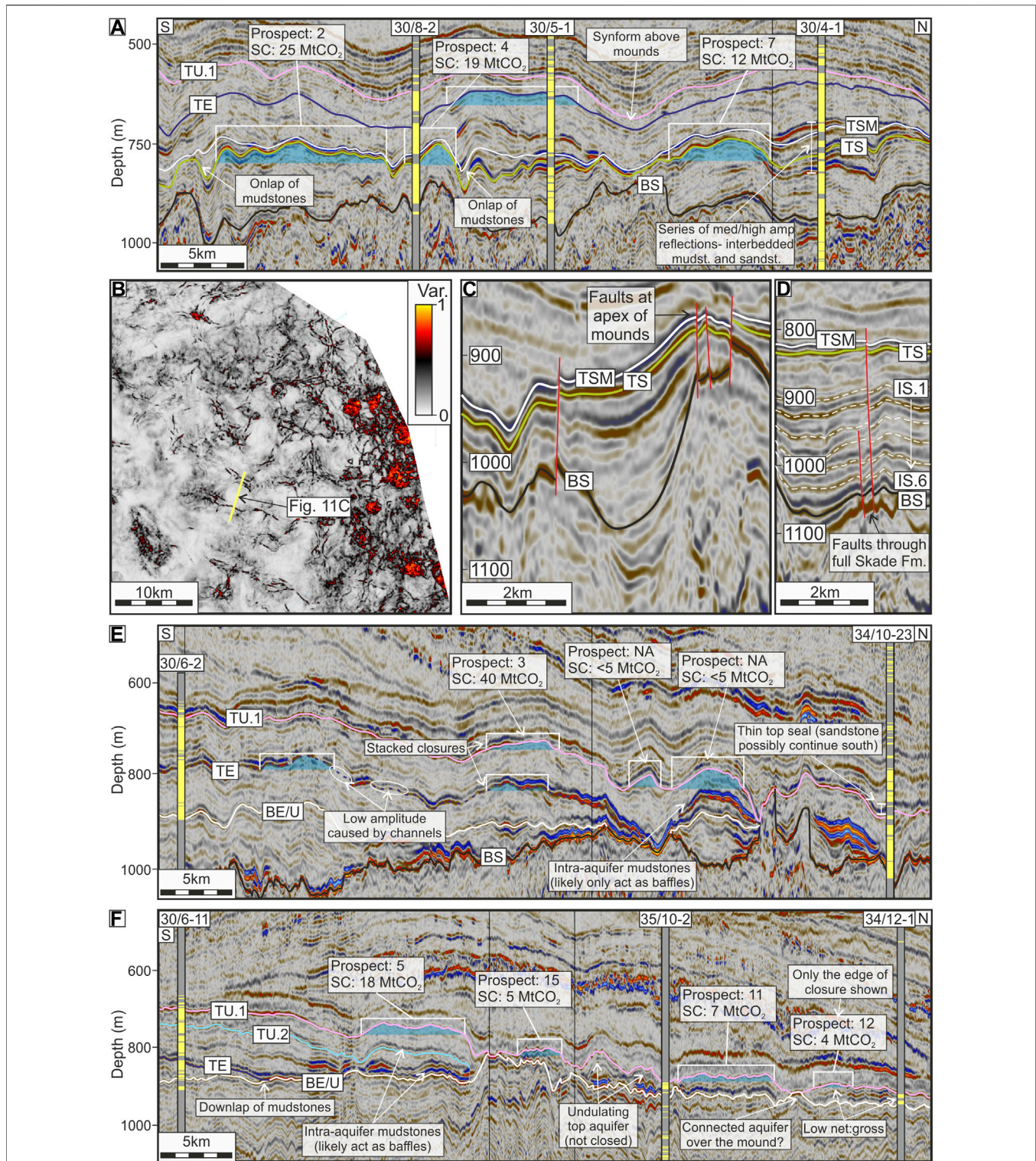
FIGURE 11 | Intra-aquifer mudstone analysis. (A) Seismic strike section showing Skade Fm. closures and variability in top Skade Fm. mudstones. **(B)** Top Skade Fm. mudstone RMS variance extraction, highlighting the faults that extend through the full mudstone. The faults are primarily located at the crest of underlying mounds. **(C)** Seismic section of the faults at mound crests that extend through the thin Skade Fm. and overlying mudstone. Line location in "**(B)**." **(D)** Seismic section of faults in the thicker regions of the Skade Fm. where only a few faults at the mound crests extend through the Skade Fm. and overlying mudstone. Line location in **Figure 10B**. **(E)** Seismic strike section showing Utsira Fm. closures and variable top Eir Fm. reflection response due to channels shown in **Figure 10C**. **(F)** Seismic dip section showing closures in the northeastern area of the Utsira Fm. SC = TSP Storage Capacity. Prospect numbers refer to the 15 largest and most viable CO₂ storage traps in **Figure 14**. Location of seismic lines and map shown in **Figure 10**. TU.1 = Top Utsira 1; TU.2 = Top Utsira 2; TE = Top Eir Fm.; TSM = Top Skade Fm. Mudstone; TS = Top Skade Fm.; IS1-7 = Intra-skade 1−7; BS = Base Skade Fm.
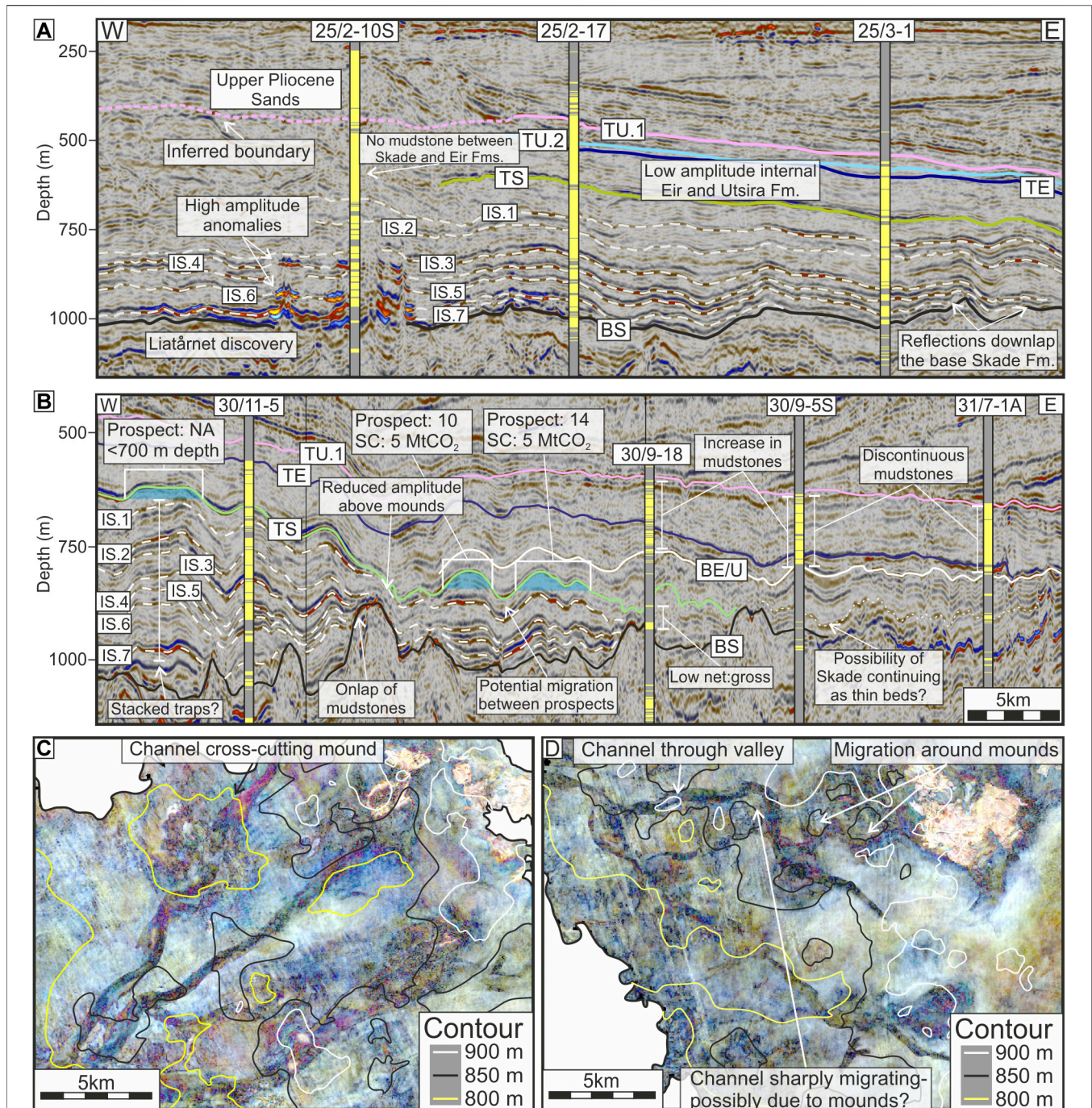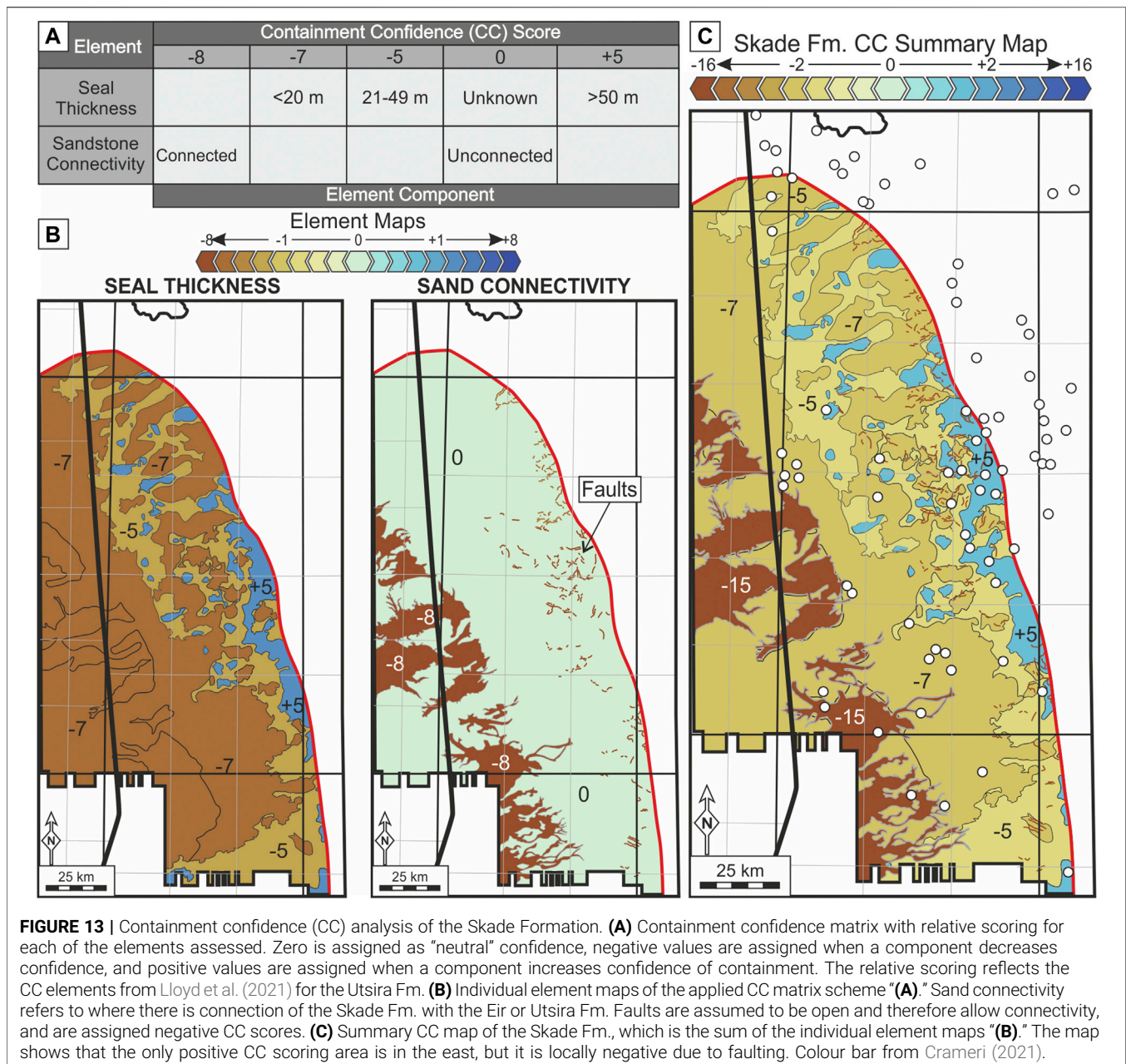
FIGURE 12 | Intra-formation mudstone analysis. (A) Seismic dip section of the intra-Skade mudstones. The Liatårnet discovery and associated amplitude anomalies are shown. Dashed pink line is where the boundary between the Upper Pliocene sandstone and Utsira Fm. is inferred. (B) Seismic dip section showing Skade Fm. closures. (C) Intra-Skade 2 (IS.2) spectral decomposition map showing channels cross-cutting mounds (shown by contours). (D) Intra-Skade 3 (IS.3) spectral decomposition map showing channels migrating around mounds and cross-cutting each other. SC = TSP Storage Capacity. Prospect numbers refer to the 15 largest and most viable CO₂ storage traps in **Figure 14**. Location of seismic lines and map shown in **Figure 10**. TU.1 = Top Utsira 1; TU.2 = Top Utsira 2; TE = Top Eir Fm.; BE/U = Base Eir/Utsira; TS = Top Skade Fm.; IS1-7 = Intra-skade 1−7; BS = Base Skade Fm.

FIGURE 13 | Containment confidence (CC) analysis of the Skade Formation. **(A)** Containment confidence matrix with relative scoring for each of the elements assessed. Zero is assigned as "neutral" confidence, negative values are assigned when a component decreases confidence, and positive values are assigned when a component increases confidence of containment. The relative scoring reflects the CC elements from Lloyd et al. (2021) for the Utsira Fm. **(B)** Individual element maps of the applied CC matrix scheme "**(A)**." Sand connectivity refers to where there is connection of the Skade Fm. with the Eir or Utsira Fm. Faults are assumed to be open and therefore allow connectivity, and are assigned negative CC scores. **(C)** Summary CC map of the Skade Fm., which is the sum of the individual element maps "**(B)**." The map shows that the only positive CC scoring area is in the east, but it is locally negative due to faulting. Colour bar from Crameri (2021).

cutting channels and their relationship to underlying mounds (**Figures 12C,D**). In the distal parts of the basin (to the east), the mudstones produce high amplitude seismic reflections. The deepest mudstones (IS. 5–7) either downlap onto the base Skade Fm., where they have reached their full extent into the basin (**Figures 7A, 12A**), or bend upwards at the mounds. Channels are not observed to extend this far into the basin at this time. The shallower mudstones (IS. 4–3) either onlap (**Figure 12B**) or drape over the mounds, where they lose their amplitude strength (**Figures 7A, 12B**). In some areas, channels appear to have been influenced by the mounds, observed to either have changed direction through deflection, or meandered around the mounds through diversion (**Figure 12D**). This implies

that the mounds were either forming during deposition or creating topography on the basin floor that steered the channels. The shallowest mudstones (IS. 1–2) drape over the mounds and contain channels that appear to cross-cut the mounds (**Figure 12C**), implying that the accommodation between topographic highs was filled and mounds were immobile at this time.

Containment Confidence Assessment for the Skade Formation

The only intra-aquifer mudstone that reached the advised minimum thickness (50 m) for a seal for CO₂ storage is the Top Skade Fm. mudstone. We apply the same common risk

segment mapping methodology to the Skade Fm. as Lloyd et al. (2021) applied to the Utsira Fm., in order to assess containment confidence (CC). However, the CC matrix has been altered to remove "Overburden Interval" elements, which correspond to the stratigraphy above the 50 m "Seal Interval," as these are already considered in the CC assessment for the Top Utsira Fm. In the Seal Interval, the "sandstone presence" matrix element (Lloyd et al., 2021) is replaced with "seal thickness," because aquifer sandstones lie directly above the mudstones. Hence, where the seal is thin (<50 m), sandstones are inherently within the Seal Interval. As there are faults extending through the Top Skade Fm. mudstone, these are incorporated into the "sandstone connectivity" element in the matrix (**Figure 13A**). The presence of the shallower Eir and Utsira Fms. above the Skade Fm. could increase containment confidence, as they act as a buffer reservoirs for vertical migration out of the Skade Fm. However, they cannot be relied upon for long-term storage, as the Top Eir Fm. is thin, and the CC score for the Utsira Fm. in the area directly above the Skade Fm. is entirely negative, due to the presence of several connected sandstones in the seal and overburden stratigraphy (Naust Fm.) (Lloyd et al., 2021).

For "seal thickness" (**Figures 13A,B**), where the mudstone thickness drops below 50 m, sandstones (the basal Eir Fm.) are within the Seal Interval, the minimum seal thickness requirement is not met and a CC score of −7 is assigned. Where the mudstone is thick (20−49 m), but does not meet the advised minimum thickness, a CC score of −5 is assigned. Where the mudstones are > 50 m thick, a CC score of +5 is assigned (**Figure 13**). This resembles the CC scoring applied to the Seal Interval of the Utsira Fm., whereby "possible," "probable" and "proven" sandstones were assigned increasingly negative CC scores and 'probable and "proven" mudstones were assigned increasingly positive CC scores (Lloyd et al., 2021). Based on this, the only area of the Skade Fm. with a positive CC score is in the distal eastern region (**Figure 13B**).

For the second element in the matrix, "sandstone connectivity," we assess for areas that could facilitate seal bypass through the mudstone, thereby connecting the Skade Fm. to the Eir and Utsira Fms. If connected, we assign the same CC score as a full connection (reservoir to seal to overburden) for the Utsira Fm. assessment (CC = −8, Figures 13, 14A in Lloyd et al., 2021). Connectivity is interpreted where the mudstone reflection is absent or dimmed relative to the surrounding, which primarily occurs due to erosion of the mudstones on or near the ESP, due to the canyons and slope channels. Faults are also observed to offset the mudstone and extend into the basal parts of the overlying aquifer (**Figures 11B,C**). There is no data constraint on the sealing potential of the faults, but to be conservative, we assume they are "open" faults and therefore connect the Skade and Eir Fms (CC = −8, **Figure 13**). For assessment of other aquifers, it could be an oversimplification to assume that the faults are open and this could lead to prospects being discounted. Membrane sealing or lithology juxtaposition across the fault conversely could lead to a fault seal. Here, no prospects were removed due to fault presence, since the only closure that was penetrated by a fault was already discounted due to low seal

thickness. However, the feasibility of other aquifers could be highly dependent on a robust fault seal analysis (Wu et al., 2021).
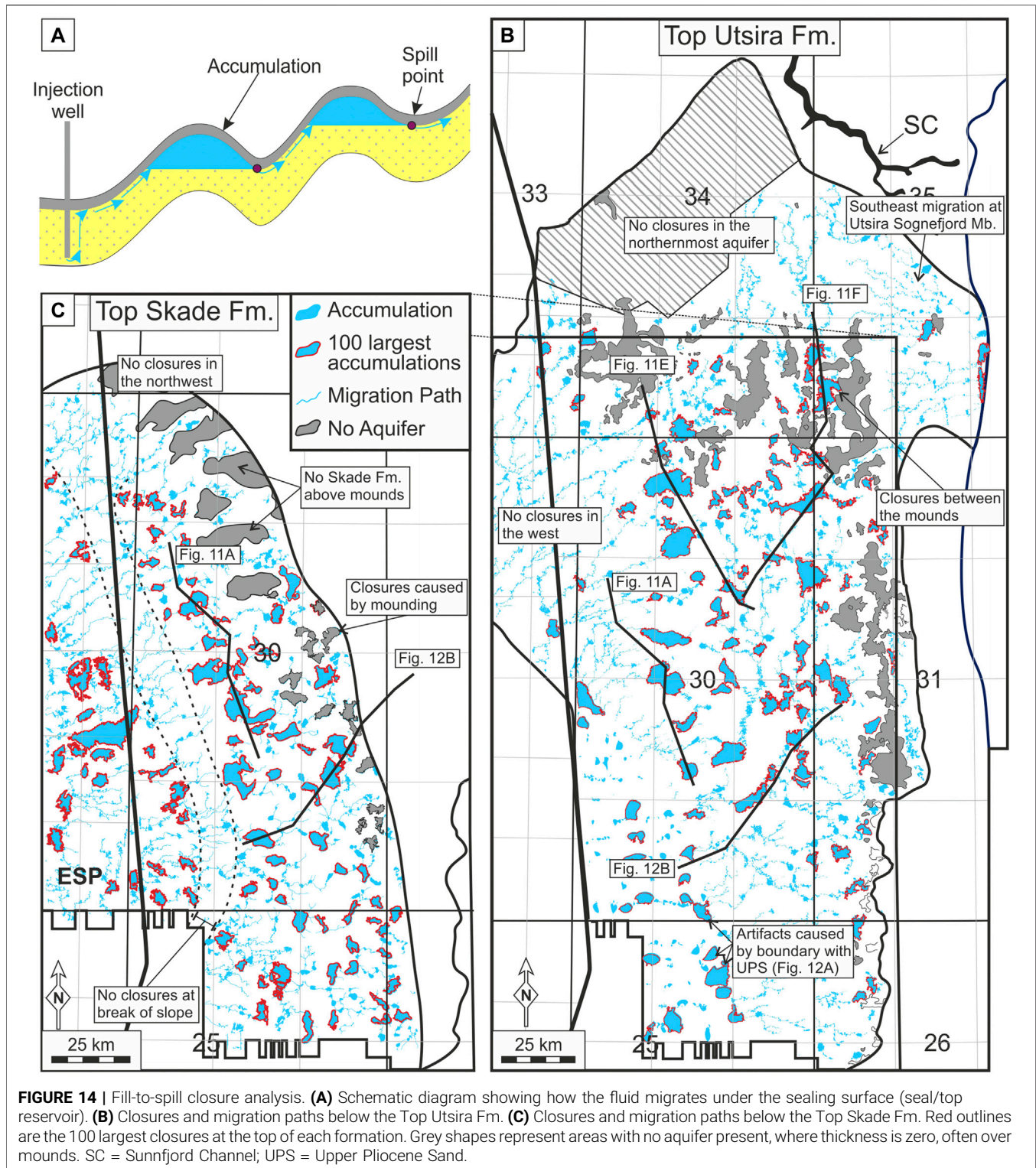
We combine the two matrix elements (seal thickness and sandstone connectivity) into a Summary CC map (**Figure 13C**). The positively scoring areas (east), are only modified by sandstone connectivity due to the faults, which are primarily located in the northern area. Therefore, the central-eastern region of the Skade Fm. has the highest containment confidence of CO₂. The western part of the Skade Fm has a negative CC score due to its low thickness and connectivity of sands (**Figure 13C**).

CO₂ Migration and Trapping

CO₂ can be immobilised via physical (structural/stratigraphic- and residual-) and chemical (dissolution- and mineral-) trapping, which have variable effectiveness over different timescales (Intergovernmental Panel on Climate Change et al., 2005). Here, we mainly consider physical trapping via structural closures; the dominant trapping mechanism 1−100 years after injection, after which other mechanisms become increasingly influential (Bachu et al., 2007). We mapped structural closures and CO₂ migration paths at the top of the Skade and Utsira Fms. Structural closures have also been identified at the top of the Eir Fm. and in the intra-Skade mudstone layers, but their low thickness and intersection by sand-filled channels (**Figure 10C**), manifesting as potential seal bypass systems, potentially limits sealing capacity. Using Permedia™'s fill-and-spill workflow (**Figure 14A**), the 100 largest structural closures in each formation were highlighted (red outlined polygons; **Figures 14B,C**). The overall geometry of the aquifer suggests a preferential up-dip migration direction towards the west. This could be of concern due to: 1) migration of CO₂ to shallower depths and thus towards conditions where CO₂ would leave the supercritical phase, and 2) high possibility of seal bypass and migration out of the reservoir, due to several connected sandstones in the seal and overburden towards the west (Lloyd et al., 2021). As such, CO₂ would likely be more secure in structural traps rather than through use of the full aquifer.

Top Utsira Fm. Closures

Beneath the Top Utsira Fm., the major closures are in the central and northern parts of the aquifer (**Figure 14B**). The structure of the top and base-aquifer surfaces in this region appear to have an inverse relationship, whereby mounds in the base aquifer surface correspond to overlying synforms in the top aquifer surface and depressions in the base aquifer surface correspond to overlying antiforms in the top aquifer surface. As a result, there are features with convex tops that form structural traps between the mounds (**Figures 11A,F**). Dipping strata towards the mounds form the limbs of many of the closures (**Figure 11F**). In map view, the closures are primarily juxtaposed against the mounds (grey shapes; **Figure 14B**). It is postulated that deflation of the mounds led to localised subsidence and formation of the coeval synforms in the aquifer and shallower stratigraphy (Kennett & Jackson, 2008). This localised subsidence and downward rotation of

FIGURE 14 | Fill-to-spill closure analysis. **(A)** Schematic diagram showing how the fluid migrates under the sealing surface (seal/top reservoir). **(B)** Closures and migration paths below the Top Utsira Fm. **(C)** Closures and migration paths below the Top Skade Fm. Red outlines are the 100 largest closures at the top of each formation. Grey shapes represent areas with no aquifer present, where thickness is zero, often over mounds. SC = Sunnfjord Channel; UPS = Upper Pliocene Sand.

the strata led to the formation of adjacent antiforms, which characterise the closures here highlighted for CO$_2$ storage. An alternative explanation is differential compaction between the mounds and depressions.

Other closures at the Top Utsira Fm. formed at undulations in the top surface that appear to be unrelated to the mounds (**Figures 11E,F**). There are few closures in the west and no major closures in the northernmost part of the Utsira Fm.

TABLE 1 | Catalogue of CO2 storage prospects. Storage capacities are given for the full reservoir thickness (FRT) of the prospect (storage efficiency 5%) and from the top to the spill point (TSP) of the trap (storage efficiency 20%). The volume percentage of the TSP relative to the FRT of the prospect (TSP:FRT) is presented for reference. Only prospects with a FRT storage capacity > 5 Mt CO2 are included. Containment Confidence (CC) score is from **Figure 13** for the Skade Fm. and Lloyd et al. (2021) (**Figure 15** therein) for the Utsira Fm. The lowest CC score within a given closure is taken, e.g., a fault through a small part of the closure reduces the CC score of the whole closure. GRV = gross rock volume; SC = storage capacity; Well Pen. = number of well penetrations.

Prospect no.	Apex depth (m)	Max. closure height (m)	Well used for N:G	Porosity (%)	Full reservoir thickness			Top to spill point			TSP:FRT (%)	CC score	Well pen.
					GRV (MM Sm³)	N:G	SC (Mt CO₂)	GRV (MM Sm³)	N:G	SC (Mt CO₂)			
Utsira formation													
1	709	37	30/2-2	35	6,930	1.00	**61**	616	1.00	**21**	8.9	−13	0
3	794	63	30/2-1	35	5,550	0.92	**45**	1,230	0.93	**40**	22.1	−13	0
5	729	40	30/3-2R	35	4,010	0.90	**32**	517	1.00	**18**	12.9	+5	0
8	819	32	34/10-23	36	2,090	0.95	**18**	285	0.91	**9**	13.6	−1	0
11	855	37	35/10-2	33	1,290	0.58	**6**	364	0.58	**7**	28.2	+4	0
12	879	30	34/12-1	33	976	0.72	**6**	164	0.72	**4**	16.8	+4	0
15	791	33	30/3-1R	34	580	0.91	**5**	172	0.94	**5**	29.7	+4	0
Skade formation													
2	730	60	30/8-2	36	5,390	0.95	**46**	781	0.9	**25**	14.5	−7	0
4	727	54	30/8-2	37	4,030	0.95	**35**	575	0.9	**19**	14.3	−7	0
6	702	63	30/7-7	36	3,830	0.76	**26**	638	0.81	**19**	16.7	−7	0
7	728	42	30/4-1	36	2,480	0.89	**20**	380	0.88	**12**	15.3	−15	0
9	768	44	30/9-13S	36	2,350	0.58	**12**	214	0.41	**3**	9.1	−7	>1
10	784	76	30/9-18	36	2,450	0.34	**8**	632	0.22	**5**	25.8	−5	0
13	908	44	30/5-1	35	679	0.86	**5**	149	0.81	**4**	21.9	−5	0
14	803	90	30/9-18	35	1,590	0.34	**5**	707	0.22	**5**	44.5	+5	>2

Bad ◄◄◄◄► Good

Storage capacities are highlighted in bold.

(**Figure 14B**). Apparent closures in the southwest are artifacts related to mapping, where the surface is cropped beneath the Upper Pliocene sandstone (**Figures 12A**, **14B**). The potential migration paths flow towards the ESP for all formations, apart from the Utsira Formation East, where there is flow potential toward the Norwegian margin (**Figure 14B**).

Top Skade Fm. Closures

Beneath the Top Skade Fm., the largest closures appear to be clustered in two areas; in a source-proximal area on the ESP (Blocks 30/7, 30/10 and UK blocks), and in a source-distal area, in the eastern and southern (Blocks 30/8, 30/9, 30/11, 30/12, 25/2 and 25/3) parts of the formation (**Figure 14C**). Closures on the ESP are formed in-between large, adjacent canyons, where surrounding erosion has left behind structural highs. Due to their shallow depth (ca. 500 m), these have been discounted. In the east, several of the closures are artifacts caused by breakthrough of the mounds through the Top Skade Fm. surface (i.e., no Skade Fm. is present). Migration paths from the distal closures appear to flow westwards, towards the ESP. There are relatively few closures on the ESP upper-slope and in the northern part of the formation (**Figure 14C**).
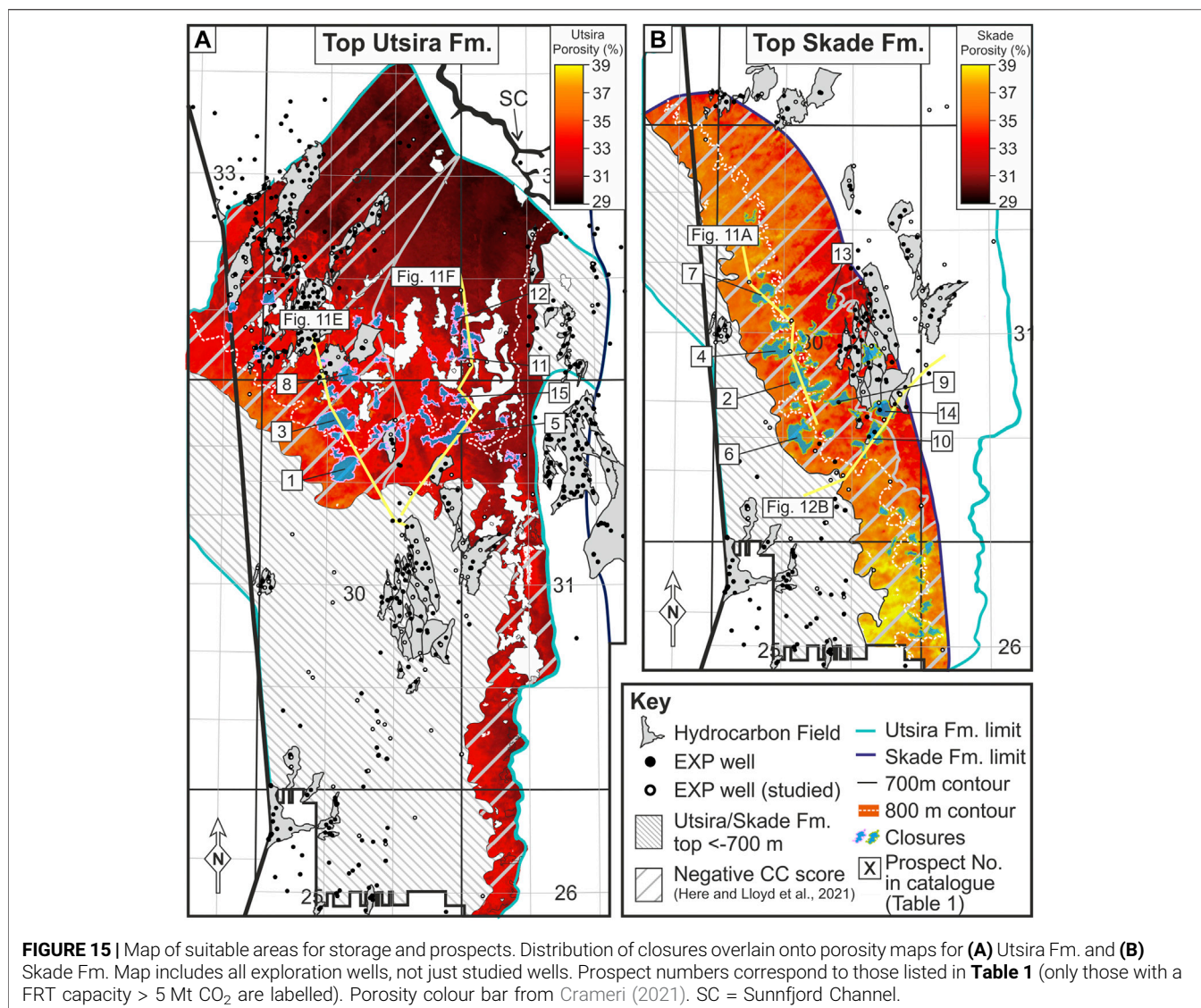
DISCUSSION

Prospect Storage Capacities

We undertook detailed assessment of prospects using both the FRT and TSP for storage capacity calculations (**Figure 3B**). Fifteen prospects have a FRT storage capacity of > 5 Mt CO₂

and apex depth > 700 m, and are detailed in the catalogue with their characteristics (apex depth, GRV, porosity, storage capacity, TSP:FRT volume percentage, number of well penetrations and containment confidence score) (**Table 1**).

The prospects are numbered according to FRT storage capacity from largest (1) to smallest (15) across both formations; seven are within the Utsira Fm. and eight in the Skade Fm. (**Table 1**). The total storage capacity of the 15 prospects is 330 Mt CO₂ (FRT) or 196 Mt CO₂ (TSP). The FRT storage capacity is unevenly distributed between individual prospects; the fifth-largest with 50% capacity (32 Mt CO₂), and the eleventh with ~10% capacity (6 Mt CO₂) of the largest prospect (61 Mt CO₂). Differences between FRT and TSP storage capacities primarily depend upon the TSP:FRT volume percentage, i.e., the proportion of GRV that is within the structural trap, relative to the full reservoir thickness of the prospect (**Table 1**). For example, only 9% of the FRT GRV of Prospect 1 is within the structural trap (TSP), yielding approximately one-third of the storage capacity for the TSP (21 Mt CO₂) relative to the FRT (61 Mt CO₂), also due to the different storage efficiencies applied and minor differences in N:G. Although Prospect 1 has the largest FRT storage capacity, due to the thick reservoir beneath the spill point of the closure (61 Mt CO₂ FRT; 21 Mt CO₂ TSP), Prospect 3 has the largest structural trap and therefore greatest TSP storage capacity (45 Mt CO₂ FRT; 40 Mt CO₂ TSP).

It should be noted that this is not a full assessment of the storage capacity of the aquifer, as we refine capacity estimates to specific prospects. Site-specific storage capacities cannot be directly compared to existing full-aquifer storage capacity

FIGURE 15 | Map of suitable areas for storage and prospects. Distribution of closures overlain onto porosity maps for **(A)** Utsira Fm. and **(B)** Skade Fm. Map includes all exploration wells, not just studied wells. Prospect numbers correspond to those listed in **Table 1** (only those with a FRT capacity > 5 Mt CO$_2$ are labelled). Porosity colour bar from Crameri (2021). SC = Sunnfjord Channel.

studies (Holloway, 1996; Bøe et al., 2002; Chadwick et al., 2008; Halland et al., 2011; Thibeau & Mucha 2011; Pham et al., 2013a; Gasda et al., 2017; Thibeau et al., 2018). We do not provide the storage capacity for areas of the aquifer outside of structural traps, even though they may have suitable properties for storage (positive CC and > 700 m depth). This is because we have not constrained the possible migration of CO$_2$ outside of structural traps within the aquifer. Given the regional structural dip, it would likely migrate south-westwards towards unfavourable areas in terms of containment (sandstones in the seal and overburden; Lloyd et al., 2021). Modelling could help to constrain migration and allow inclusion of more of the aquifer through a fill-to-spill injection approach, which would increase the total GRV and the total storage capacity. Dynamic modelling in the southern Utsira Fm. (beyond the southern limit of this study), where 125 Mt CO$_2$ was injected, found that CO$_2$ will migrate up to 33 km from an injection point during a 5,000 year period, either becoming

physically trapped or immobilised (Bergmo et al., 2009). However, the mineral trapping potential of the Utsira Fm. is considered to be limited, as reactive mineral phases are minor constituents of the formation (Johnson et al., 2004; Audigane et al., 2007; Thibeau et al., 2007; Pham et al., 2013b).

Catalogue of CO$_2$ Storage Sites

Carbon Dioxide needs to be in a supercritical phase for subsurface storage, where the fluid has the viscosity of gas, but the density of a liquid (Span & Wagner, 1996). CO$_2$ enters the supercritical phase at 31°C and 73.8 bar pressure (Span & Wagner, 1996). If CO$_2$ is injected and stored at shallower depths, CO$_2$ would be in gaseous phase, which would be less dense and require greater storage capacity (International Energy Agency, 2008). In the Norwegian North Sea, optimal conditions are expected at depths > 700–800 m below sea level (Halland et al., 2011; Pham et al., 2013a) and we used

700 m as the depth criteria in the prospect assessments (apex depth, **Figure 15**; **Table 1**). Considering the two formations deemed suitable for storage based on containment confidence analysis (Skade and Utsira Fms.), the specific areas most suitable for storage (and within which closures are mapped) are the northernmost part of the aquifer (Utsira Fm.) and the central part of the aquifer (eastern part of the Skade Fm.) (**Figure 15**).

For a storage site to be suitable, it needs to have sufficient capacity (**Section 6.1**) and confidence in containment of CO₂. In the catalogue (**Table 1**), we show the fifteen identified prospects with their associated Containment Confidence score (CC score), calculated in this study for the Skade Fm. (**Figure 13**) and from Lloyd et al. (2021) for the Utsira Fm. The elements considered towards the CC score for each formation differ depending on the geology of the seal (and overburden for the Utsira Fm) and the data available. The main uncertainties with the CC matrix are discussed in Lloyd et al. (2021). If only prospects in the positive CC scoring regions for both the Utsira Fm. and Skade Fm. are considered, then only five of the fifteen prospects can be used (four in the Utsira Fm. and one in the Skade Fm.). This reduces the total FRT storage capacity of the prospects from 330 to 54 Mt CO₂ (196−39 Mt CO₂ TSP), with 49 Mt CO₂ (FRT) within the Utsira Fm. and only 5 Mt CO₂ (FRT) in the Skade Fm. Many of the structural traps identified in the Skade Fm. are situated towards the west, where we have interpreted low (negative) containment confidence due to < 50 m seal thickness (**Figures 13, 15B**). Conversely, the structural traps towards the east (in the Skade pinch-out zone), where we interpreted high (positive) containment confidence (>50 m seal thickness), suffer from a low N:G, due to their more distal position relative to the sediment source. If a more optimistic seal thickness (thinner) requirement were to be used (perhaps constrained through seal integrity analyses), further of the Skade Fm. prospects could fall within a positive CC scoring area. These prospects also have a higher N:G (**Table 1**), hence the total storage capacity could be greatly improved through a greater understanding of the sealing potential of the mudstones. The number of well penetrations at each closure was also noted (**Figure 15**), as they may also compromise containment. The north-eastern area that is deemed suitable for storage within the Utsira Fm. (**Figure 15**) is relatively underexplored for hydrocarbons and has few well penetrations; none penetrating the identified prospects. However, the only prospect with a positive CC score in the Skade Fm. is situated close to producing fields (e.g., Oseberg) and has several (>2) well penetrations.

For the Utsira Fm., the most promising prospect, with zero well penetrations and a positive CC score is Prospect 5, with a storage capacity of 32 Mt CO₂ (FRT) or 18 Mt CO₂ (TSP) (**Figure 15A**; **Table 1**). There are three other prospects that satisfy these criteria: Prospects 11, 12 and 15. The largest prospects in terms of storage capacity across both formations (Prospects 1−4) account for 187 Mt CO₂ (FRT) or 105 Mt CO₂ (TSP) capacity, but have negative CC scores, due to their thin (<50 m) mudstone seals.

Comparing the prospects across the two formations, although they are at similar depths and the Utsira Fm. generally has higher average porosity than the Skade Fm., the prospects in the Skade Fm. have a higher average porosity (36%) than those in the Utsira Fm. (34%). This is likely due to the more distal position of the suitable part of the Utsira Fm. from the sediment source, where pore size is reduced from increased clay content and greater compaction (Yang & Aplin, 2004). The total storage capacity for identified prospects in the catalogue is 173 Mt CO₂ (FRT) or 104 Mt CO₂ (TSP) in the Utsira Fm., compared to 157 Mt CO₂ (FRT) or 92 Mt CO₂ (TSP) in the Skade Fm. (**Table 1**). There are no regions (at a suitable depth) where Utsira Fm. and Skade Fm. prospects are vertically-stacked and could be targeted with a single well. However, although not presented in **Figure 15**, smaller traps (<5 Mt CO₂ FRT capacity; **Figure 14**) could be utilised through a lateral network with a single injector well and a "fill-to-spill" approach.

Intra-Formational Barriers or Baffles

In this study we have highlighted and assessed intra-formation mudstones, however we raise doubts over their ability to trap fluid primarily due to cross-cutting, possibly sand-filled channels, but also faulting, that could allow for seal bypass. Other seal bypass mechanisms that also need to be considered are demonstrated at other local sites. At the Sleipner injection site (Utsira Fm.), eight intra-formation mudstones were identified prior to CO₂ injection (Chadwick et al., 2004). These internal baffles were expected to result in slower migration of the CO₂ plume, through accumulation of fluid and eventual breaching of each baffle over time when the pore pressure exceeds the capillary entry pressure. However, after only 3 years of injection, CO₂ was detected in the sandstones directly beneath the cap rock (Cavanagh & Haszeldine, 2014). The cause has been suggested to be sub-seismic features that allowed bypass of the mudstones such as microfractures, faults, sand injectites, carbonate cement dissolution, lateral discontinuities, chimney excavation, or erosive holes created by high-energy deposition (Zweigel et al., 2004; Hermanrud et al., 2009; 2010). Hydro-fracturing of thin shales caused by fluctuation of ice loads through the Quaternary glaciations has also been suggested (Cavanagh & Haszeldine, 2014); a mechanism that would affect all thin shales in this stratigraphic interval across the North Sea. Although these mudstones did not act as barriers to flow, each mudstone was found to hold some of the CO₂ column beneath it, thereby reducing the lateral extent of the plume during injection (Chadwick et al., 2004; Cavanagh & Haszeldine, 2014). It is expected that by the end of injection, 40% of the CO₂ will be residually-trapped (Hermanrud et al., 2009), with some of the CO₂ draining to the top of the Utsira Fm., rendering the intra-formation mudstones less important with time (Chadwick et al., 2004).

Elsewhere, intra-formation mudstones have trapped fluids at the site of the recent Liatårnet oil discovery at the base of the Skade Fm. (**Figure 11A**). A Christmas tree-like structure is apparent, whereby a central pipe of low amplitude, chaotic

reflections is flanked by a series of high amplitude limbs. The pipe is interpreted as a fluid migration chimney that breached the lower mudstones, and the high amplitudes are interpreted as small, leaked hydrocarbon accumulations that sit under each of several overlying mudstone layers. Further upward migration through overlying sandstones is possible, but not clear from the seismic data. There is also no indication for the timing of hydrocarbon "leakage," and it can be inferred that either the rate of migration into the reservoir is greater than hydrocarbon leakage through the seal and overburden, or that the hydrocarbon leakage only breached the lower mudstones. Although there is some comparison to mudstone breaching at Sleipner, it is important to consider the difference between hydrocarbon migration over geological time and CO$_2$ migration over decadal timescales. Nonetheless, despite the chimney, intra-formation mudstone layers are proven to ultimately trap fluid at Liatårnet, although other sealing lithologies may also contribute (e.g. cemented sandstones).

The Way Forward—Testing the Feasibility of CO$_2$ Storage Sites

We have undertaken a detailed assessment of the northern Utsira-Skade Aquifer for CO$_2$ storage, and identified several structural traps and potential prospects. In order for these to have a practical application, several further steps are required, including: 1) dynamic modelling of CO$_2$ injection, to understand the role of other trapping mechanisms and migration to smaller closures, 2) geomechanical testing of the cap rock, to assess the seal integrity and possibly upgrade areas with low CC scores; and 3) pressure analysis through the aquifer. The data required for each of these could be collected through drilling of a CO$_2$ storage exploration well. Independent CO$_2$ storage wells are costly and uneconomic in the currently limited market. The only CO$_2$ storage well to date on the Norwegian Continental Shelf (31/5-7 Eos) was drilled with significant government subsidy. However, the CO$_2$ storage prospects identified here (along with other North Sea aquifers with CO$_2$ storage potential), lie in a mature hydrocarbon province. Thus, the economics of a CO$_2$ storage project could be improved through dual-objective wells, which target and test both CO$_2$ storage and hydrocarbon prospects in the same well. Although the Utsira Fm. prospects are located towards the centre of the NVG, away from any existing fields, the prospects in the Skade Fm. are near the Oseberg Field, so could possibly be targeted through infrastructure-led exploration/near-field wells. Hydrocarbon demand is reducing, and exploration is expected to decline in the coming decades, as the energy industry transitions towards low carbon energy sources. We advocate that impending hydrocarbon wells on the NCS should be drilled with CO$_2$ storage in mind through their data acquisition programmes. With more data, the characterisation of the potential aquifers will be improved and CO$_2$ storage operations will be made safer. With a CO$_2$ storage-focussed drilling programme on the NCS coupled with that for hydrocarbons, fewer independent CO$_2$ storage exploration wells may ultimately be required. This incentive could prompt further

investment in CO$_2$ storage on the NCS and allow entry to smaller competitors. With several robust options for storage, the market will have greater opportunity to develop.

CONCLUSION

The Utsira-Skade Aquifer in the northern North Sea is already used for CO$_2$ storage in its southern region at the Sleipner injection site. If CCS is upscaled for countries and businesses to reach their climate goals, additional storage sites will be required and the area bordering the first CO$_2$ storage licence (our study area) on the NCS could be prospective. This study combined 3D regional seismic data, FWI velocity data and 102 exploration wells and analysed the CO$_2$ storage potential of the northern Utsira-Skade Aquifer (Utsira, Skade and Eir Fms.), providing a catalogue of CO$_2$ storage sites.

Intra-reservoir heterogeneities (average porosity and mudstone baffles and barriers) were assessed and mapped. Average porosity for the aquifer was calculated by applying a function derived from well data to the FWI velocity cube and ranges from 29 to 39% (37% for the Utsira/Eir Fms. and 33% for the Skade Fm.), generally decreasing away from the East Shetland Platform. The thickest mudstone (>50 m), interpreted to be a regional barrier, is located towards the centre of the aquifer, separating the Skade Fm. from the overlying Eir and Utsira Fms., and thins to the west. Several intra-formation mudstones were mapped, primarily in the Skade Fm., but are interpreted to be baffles (not barriers) to flow, due to their low thickness (<10 m). Structural closures were mapped at both the top aquifer (Utsira Fm.) and top Skade Fm. surfaces. CO$_2$ storage capacity was calculated for the structural traps (top to spill point of the closures, TSP) using a storage efficiency of 20%, and for the full reservoir thickness (FRT) beneath the closures, using a storage efficiency of 5%. Moreover, spill-points of the closures were mapped locally and generally reveal possible fluid migration paths to the west. Finally, containment confidence (CC) of the prospects was integrated and used to discuss the suitability of the identified prospects for storage.

Structural closures at a depth > 700 m and with FRT storage capacity > 5 Mt CO$_2$ are considered to be prospects and were assessed. A catalogue of fifteen prospects is presented for the northeastern Utsira Fm. and the central-eastern Skade Fm, with a combined storage capacity of 330 Mt CO$_2$ (FRT) or 196 Mt CO$_2$ (TSP). Of the fifteen prospects, only five have a positive CC score and they have a combined storage capacity of 54 Mt CO$_2$ (FRT) or 39 Mt CO$_2$ (TSP). The two prospects with the highest storage capacity in the Utsira Fm. have negative CC scores. The third-largest prospect has a positive CC score, zero well penetrations and a storage capacity of 32 Mt CO$_2$ FRT or 18 Mt CO$_2$ TSP. The CC score of the larger prospects could improve with more detailed understanding of the seal rocks, which could upgrade their feasibility for storage. Although there were no vertically-stacked traps identified between the Utsira, Eir and Skade Fms., detailed understanding of the timing of fill-and-spill between laterally-adjacent closures

would enable smaller closures outside of the catalogue to be utilised, and injection to be optimised.

We have undertaken a detailed evaluation of CO_2 storage sites, with an exploration-scale dataset. For further appraisal, core material would need to be acquired for analysis of caprock integrity and mineralogy. Pressure is also a crucial parameter to understand and warrants specific testing. This information can be obtained through further drilling, which could attract cost-savings by "piggy-backing" hydrocarbon exploration wells. Future work should involve dynamic modelling of the two regions suitable for storage for a fuller understanding of potential flow dynamics, to include physical and chemical trapping, with different constraints on injection and timing.

DATA AVAILABILITY STATEMENT

The data analysed in this study is subject to the following licenses/restrictions: Seismic survey is property of CGG. FMB is property of TGS. Other well data is openly available from NPD. Requests to access these datasets should be directed to https://www.cgg.com/multi-client-data/multi-client-seismic/ northern-viking-graben and https://www.tgs.com/products-services/well-data/interpretation/facies-map-browser.

AUTHOR CONTRIBUTIONS

CL: principle investigator and main author. MH: discussion, manuscript review and project organiser BB: discussion and manuscript review AN: discussion and manuscript review.

REFERENCES

CONFLICT OF INTEREST

Author BB was employed by the company Equinor ASA.

The remaining authors declare that the research was conducted in the absence of any commercial or financial relationships that could be construed as a potential conflict of interest.

Anell I., Thybo H., and Rasmussen E. (2012). A Synthesis of Cenozoic Sedimentation in the North Sea. *Basin Res.* 24, 154–179. doi:10.1111/j.1365-2117.2011.00517.x

Audigane P., Gaus I., Czernichowski-Lauriol I., Pruess K., and Xu T. (2007). Two-dimensional Reactive Transport Modeling of CO2 Injection in a saline Aquifer at the Sleipner Site, North Sea. *Am. J. Sci.* 307, 974–1008. doi:10.2475/07.2007.02

Bachu S., Bonijoly D., Bradshaw J., Burruss R., Holloway S., Christensen N. P., et al. (2007). CO2 Storage Capacity Estimation: Methodology and Gaps. *Int. J. greenhouse gas Control* 1, 430–443. doi:10.1016/s1750-5836(07)00086-2

Bachu S. (2015). Review of CO2 Storage Efficiency in Deep saline Aquifers. *Int. J. Greenhouse Gas Control.* 40, 188–202. doi:10.1016/j.ijggc.2015.01.007

Batchelor C. L., Ottesen D., and Dowdeswell J. A. (2017). Quaternary Evolution of the Northern North Sea Margin through Glacigenic Debris-Flow and Contourite Deposition. *J. Quat. Sci.* 32, 416–426. doi:10.1002/jqs.2934

Bergmoa P. S., Grimstad A.-A., Lindeberg E., Riis F., and Johansen W. T. (2009). Exploring Geological Storage Sites for CO2 from Norwegian Gas Power Plants: Utsira South. *Energ. Proced.* 1, 2953–2959. doi:10.1016/j.egypro.2009.02.071

Intergovernmental Panel on Climate Change (2005). "Special Report on Carbon Dioxide Capture and Storage," in *Prepared by Working Group III of the Intergovernmental Panel on Climate Change*. Editors B. Metz, O. Davidson, H. C. de Coninck, M. Loos, and L. A. Meyer

(Cambridge, United Kingdom and New York, NY, USA: Cambridge University Press), 442.

Bøe R., Magnus C., Osmundsen P. T., and Rindstad B. I. (2002). *CO2 point Sources and Subsurface Storage Capacities for CO2 in Aquifers in Norway*. Trondheim, Norway: Geological Survey of Norway (Norges geologiske undersøkelse).

Cavanagh A. J., and Haszeldine R. S. (2014). The Sleipner Storage Site: Capillary Flow Modeling of a Layered CO2 Plume Requires Fractured Shale Barriers within the Utsira Formation. *Int. J. Greenhouse Gas Control.* 21, 101–112. doi:10.1016/j.ijggc.2013.11.017

Chadwick A., Arts R., Bernstone C., May F., Thibeau S., and Zweigel P. (2008). *Best Practice for the Storage of CO2 in saline Aquifers, Observations and Guidelines from the SACS and CO2STORE Projects*. Keyworth, Nottingham: BGS Occasional Publication No., 14.

Chadwick R. A., Kirby G. A., Holloway S., Gregersen U., Johannessen P. N., Zweigel P., et al. (2002). *Saline Aquifer CO2 Storage (SACS2). Final Report, Geological Characterisation of the Utsira Sand Reservoir and Caprocks (Work Area 1)*. Nottingham, UK: British Geological Survey.

Chadwick R. A., Zweigel P., Gregersen U., Kirby G. A., Holloway S., and Johannessen P. N. (2004). Geological Reservoir Characterization of a CO2 Storage Site: The Utsira Sand, Sleipner, Northern North Sea. *Energy* 29, 1371–1381. doi:10.1016/j.energy.2004.03.071

Crameri F. (2021). *Scientific Colour Maps: Perceptually Uniform and Colour-Blind Friendly*. Zenodo.

Davies R. J., Huuse M., Hirst P., Cartwright J., and Yang Y. (2006). Giant Clastic Intrusions Primed by Silica Diagenesis. *Geol* 34, 917–920. doi:10.1130/g22937a.1

Daynac N., Lacaze S., and Pauget F. (2016). *Interpretation of Complex Faulted Deposits in the North Sea Using the Relative Geological Time Model*. First Break. Houten, Netherlands: EAGE, 34.

De Schepper S., and Mangerud G. (2017). Age and Palaeoenvironment of the Utsira Formation in the Northern North Sea Based on marine Palynology. *Norwegian J. Geology/Norsk Geologisk Forening* 97, 1. doi:10.17850/njg97-4-04

Den Hartog Jager D., Giles M. R., and Griffiths G. R. (1993). "January. Evolution of Paleogene Submarine Fans of the North Sea in Space and Time," in Geological Society, London, Petroleum Geology Conference Series (London, UK: Geological Society of London), 59–71. doi:10.1144/0040059

Eberhart-Phillips D., Han D. H., and Zoback M. D. (1989). Empirical Relationships Among Seismic Velocity, Effective Pressure, Porosity, and clay Content in sandstone. *Geophysics* 54 (1), 82–89. doi:10.1016/0148-9062(89)91047-4

Eidvin T. (2009). *A Biostratigraphic, Strontium Isotopic and Lithostratigraphic Study of the Upper Part of Hordaland Group and Lower Part of Nordland Group in Well 34/7-2, 34/7e12 and 34/7-R-1 H from the Tordis Field in the Tampen Area (Northern North Sea)*. Stavanger, Norway: Norwegian Petroleum Directorate (NPD).

Eidvin T., Riis F., Rasmussen E. S., and Rundberg Y. (2013). Investigation of Oligocene to Lower Pliocene Deposits in the Nordic Offshore Area and Onshore Denmark. *NPD Bull.* 10, 62.

Eidvin T., Riis F., and Rasmussen E. S. (2014). Oligocene to Lower Pliocene Deposits of the Norwegian continental Shelf, Norwegian Sea, Svalbard, Denmark and Their Relation to the Uplift of Fennoscandia: A Synthesis. *Mar. Pet. Geology.* 56, 184–221. doi:10.1016/j.marpetgeo.2014.04.006

Eidvin T., and Rundberg Y. (2001). Late Cainozoic Stratigraphy of the Tampen Area (Snorre and Visund fields) in the Northern North Sea, with Emphasis on the Chronology of Early Neogene Sands. *Norwegian J. Geology.* 81, 119–160.

Eidvin T., and Rundberg Y. (2007). Post-eocene Strata of the Southern Viking Graben, northern North Sea; Intergrated Biostratigraphic, Strontium Isotopic and Lithostratigraphic Study. *Nor. J. Geol.* 87, 391–450.

EMODnet Bathymetry Consortium (2018). *EMODnet Digital Bathymetry (DTM 2018)*. EMODnet Bathymetry Consortium. Available at: https://www.emodnet-bathymetry.eu/.

European-Commission (2018). "A Clean Planet for All: A European Long-Term Strategic Vision for a Prosperous, Modern, Competitive and Climate Neutral Economy," in *In-depth Analysis in Support of the Commission Communication COM 773* (Brussels: European Commission).

Faleide J. I., Kyrkjebø R., Kjennerud T., Gabrielsen R. H., Jordt H., Fanavoll S., et al. (2002). Tectonic Impact on Sedimentary Processes during Cenozoic Evolution of the Northern North Sea and Surrounding Areas. *Geol. Soc. Lond. Spec. Publications* 196, 235–269. doi:10.1144/gsl.sp.2002.196.01.14

Færseth R. B. (1996). Interaction of Permo-Triassic And Jurassic Extensional Fault-Blocks During The Development of The Northern North Sea. *J. Geo. Soc.* 153, 931–944. doi:10.1144/gsjgs.153.6.0931

Fossen H., Schultz R. A., Rundhovde E., Rotevatn A., and Buckley S. J. (2010). Fault Linkage and Graben Stepovers in the Canyonlands (Utah) and the North Sea Viking Graben, with Implications for Hydrocarbon Migration and Accumulation. *Bulletin* 94, 597–613. doi:10.1306/10130909088

Galloway W. E., Garber J. L., Liu X., and Sloan B. J. (1993). "January. Sequence Stratigraphic and Depositional Framework of the Cenozoic Fill, Central and Northern North Sea Basin," in Geological Society, London, Petroleum Geology Conference Series (London, UK: Geological Society of London), 33–43. doi:10.1144/0040033

Galloway W. E. (2002). Paleogeographic Setting and Depositional Architecture of a Sand-Dominated Shelf Depositional System,

Miocene Utsira Formation, North Sea Basin. *J. Sediment. Res.* 72, 476–490. doi:10.1306/110801720476

Gasda S. E., Wangen M., Bjørnarå T. I., and Elenius M. T. (2017). Investigation of Caprock Integrity Due to Pressure Build-Up during High-Volume Injection into the Utsira Formation. *Energ. Proced.* 114, 3157–3166. doi:10.1016/j.egypro.2017.03.1444

Gorecki C. D., Sorensen J. A., Bremer J. M., Knudsen D., Smith S. A., Steadman E. N., et al. (2009). "Development of Storage Coefficients for Determining the Effective CO2 Storage Resource in Deep saline Formations," in SPE International Conference on CO2 Capture, Storage, and Utilization (San Diego, CA, USA: Society of Petroleum Engineers). doi:10.2118/126444-ms

Gołędowski B., Nielsen S. B., and Clausen O. R. (2012). Patterns of Cenozoic Sediment Flux from Western Scandinavia. *Basin Res.* 24, 377–400. doi:10.1111/j.1365-2117.2011.00530.x

Gregersen U., and Johannessen P. N. (2007). Distribution of the Neogene Utsira Sand and the Succeeding Deposits in the Viking Graben Area, North Sea. *Mar. Pet. Geology.* 24, 591–606. doi:10.1016/j.marpetgeo.2007.04.006

Halland E., Johansen W., and Riis F. (2011). *CO$_2$ Storage Atlas, Norwegian North Sea*. Stavanger, Norway: Norwegian Petroleum Directorate (NPD).

Hayes P., Twigger L., Ubik K., Latter T., Purcell C., Xiao B., et al. (2018). Increasing Resolution in the North Sea. *First Break* 36, 105–111. doi:10.3997/1365-2397.n0141

Hermanrud C., Andresen T., Eiken O., Hansen H., Janbu A., Lippard J., et al. (2009). Storage of CO2 in saline Aquifers-Lessons Learned from 10 Years of Injection into the Utsira Formation in the Sleipner Area. *Energ. Proced.* 1, 1997–2004. doi:10.1016/j.egypro.2009.01.260

Hermanrud C., Christensen E., Haugvaldstad M., Røynestad L. M., Tjensvold I. T., and Watsend L. (2019). *Triggers of Sand Remobilization in Deep marine Deposits*. London, UK: Geological Society London, 493.

Hermanrud C., Teige G. M. G., Iding M., Eiken O., Rennan L., and Østmo S. (2010). "Differences between Flow of Injected CO2 and Hydrocarbon Migration," in Geological Society, London, Petroleum Geology Conference Series (London, UK: Geological Society of London), 1183–1188. doi:10.1144/0071183

Holloway S. (1996). *The Underground Disposal of Carbon Dioxide, Final Report of Joule 2, Project No. CT92-0031*. Keyworth, Nottingham, UK: British Geological Survey, 355pp.

Huuse M., Duranti D., Steinsland N., Guargena C. G., Prat P., Holm K., et al. (2004). Seismic Characteristics of Large-Scale Sandstone Intrusions in the Paleogene of the South Viking Graben, UK and Norwegian North Sea. *Geol. Soc. Lond. Mem.* 29, 263–278. doi:10.1144/gsl.mem.2004.029.01.25

Huuse M., and Mickelson M. (2004). Eocene sandstone Intrusions in the Tampen Spur Area (Norwegian North Sea Quad 34) Imaged by 3D Seismic Data. *Mar. Pet. Geology.* 21, 141–155. doi:10.1016/j.marpetgeo.2003.11.018

International Energy Agency (2008). *Geologic Storage of Carbon Dioxide, Staying Safely Underground, CO2CRC*. Booklet: The Cooperative Research Centre for Greenhous Gas Technologies.

Isaksen D., and Tonstad K. (1989). *A Revised Cretaceous and Tertiary Lithostratigraphic Nomenclature for the Norwegian North Sea*. Stavanger, Norway: Norwegian Petroleum Directorate (NPD).

Johnson J. W., Nitao J. J., and Knauss K. G. (2004). Reactive Transport Modelling of CO2 Storage in saline Aquifers to Elucidate Fundamental Processes, Trapping Mechanisms and Sequestration Partitioning. *Geol. Soc. Lond. Spec. Publications* 233, 107–128. doi:10.1144/gsl.sp.2004.233.01.08

Johnson J. W., Nitao J. J., Steefel C. I., and Knauss K. G. (2001). "Reactive Transport Modeling of Geologic CO2 Sequestration in saline Aquifers: the Influence of Intra-aquifer Shales and the Relative Effectiveness of Structural, Solubility, and mineral Trapping during Prograde and Retrograde Sequestration," in First National Conference on Carbon Sequestration (Livermore, CA, USA: Lawrence Livermore National Laboratory), 14–17.

Jordt H., Faleide J. I., Bjørlykke K., and Ibrahim M. T. (1995). Cenozoic Sequence Stratigraphy of the central and Northern North Sea Basin: Tectonic Development, Sediment Distribution and Provenance Areas. *Mar. Pet. Geology*. 12, 845–879. doi:10.1016/0264-8172(95)98852-v

Jordt H., Thyberg B. I., and Nøttvedt A. (2000). Cenozoic Evolution of the central and Northern North Sea with Focus on Differential Vertical Movements of the basin Floor and Surrounding Clastic Source Areas. *Geol. Soc. Lond. Spec. Publications* 167, 219–243. doi:10.1144/gsl.sp.2000.167.01.09

Kennett C., and Jackson C. A. (2008). *Evaluation of Internal Geometries within the Miocene Utsira Formation to Establish the Geological Concept of Observed CO2 Responses on 4D Seismic in the Sleipner Area, North Sea*. London: Doctoral dissertation, Department of Earth Science and Engineering, Imperial College London.

Larsen M., Bech N., Bidstrup T., Christensen N. P., and Biede O. (2007). Kalundborg Case Study, a Feasibility Study of CO$_2$ Storage in Onshore saline Aquifers. *Danmarks og Gronlands Geologiske Undersogelse Rapport* 2, 79.

Lee M. W. (2003). "Elastic Properties of Overpressured and Unconsolidated Sediments," in *U.S. Geological Survey Bulletin*. doi:10.3133/b2214

Lindeberg E., Vuillaume J.-F., and Ghaderi A. (2009). Determination of the CO2 Storage Capacity of the Utsira Formation. *Energ. Proced.* 1, 2777–2784. doi:10.1016/j.egypro.2009.02.049

Lloyd C., Huuse M., Barrett B. J., Stewart M. A., and Newton A. M. W. (2021). A Regional CO 2 Containment Assessment of the Northern Utsira Formation Seal and Overburden, Northern North Sea. *Basin Res*. 33, 1985–2017. doi:10.1111/bre.12545

Lonergan L., Cartwright J., and Jolly R. (1998). The Geometry of Polygonal Fault Systems in Tertiary Mudrocks of the North Sea. *J. Struct. Geology*. 20, 529–548. doi:10.1016/s0191-8141(97)00113-2

Løseth H., Dowdeswell J. A., Batchelor C. L., and Ottesen D. (2020). 3D Sedimentary Architecture Showing the Inception of an Ice Age. *Nat. Commun.* 11, 2975–2977. doi:10.1038/s41467-020-16776-7

Løseth H., Raulline B., and Nygård A. (2013). Late Cenozoic Geological Evolution of the Northern North Sea: Development of a Miocene Unconformity Reshaped by Large-Scale Pleistocene Sand Intrusion. *J. Geol. Soc.* 170, 133–145. doi:10.1144/jgs2012-093err

Løseth H., Wensaas L., Arntsen B., and Hovland M. (2003). "Gas and Fluid Injection Triggering Shallow Mud Mobilization in the Hordaland Group, North Sea," in *Subsurface Sediment Mobilization*. Editors P. Van Rensbergen, R. R. Hillis, A. J. Maltman, and C. K. Morley (London, UK: Geological Society London), 139–157.

Martinsen O. J., Bøen F., Charnock M. A., Mangerud G., and Nøttvedt A. (1999). Cenozoic Development of the Norwegian Margin 60-64°N: Sequences and Sedimentary Response to Variable basin Physiography and Tectonic Setting. *Pet. Geology. Conf. Ser.* 5, 293–304. doi:10.1144/0050293

May F., Müller C., and Bernstone C. (2005). How Much CO2 Can Be Stored in Deep saline Aquifers in Germany?. *VGB powertech* 85, 32–37.

Okwen R., Yang F., and Frailey S. (2014). Effect of Geologic Depositional Environment on CO2 Storage Efficiency. *Energ. Proced.* 63, 5247–5257. doi:10.1016/j.egypro.2014.11.556

Ottesen D., Batchelor C. L., Dowdeswell J. A., and Løseth H. (2018). Morphology and Pattern of Quaternary Sedimentation in the North Sea Basin (52-62°N). *Mar. Pet. Geology*. 98, 836–859. doi:10.1016/j.marpetgeo.2018.08.022

Ottesen D., Dowdeswell J. A., and Bugge T. (2014). Morphology, Sedimentary Infill and Depositional Environments of the Early Quaternary North Sea Basin (56°-62°N). *Mar. Pet. Geology*. 56, 123–146. doi:10.1016/j.marpetgeo.2014.04.007

Ottesen D., Dowdeswell J. A., Rise L., and Bugge T. (2012). Large-scale Development of the Mid-Norwegian Shelf over the Last Three Million Years and Potential for Hydrocarbon Reservoirs in Glacial

Sediments. *Geol. Soc. Lond. Spec. Publications* 368, 53–73. doi:10.1144/sp368.6

Patchett J. G., Wiley R., and El Bahr M. (1993). "Modeling the Effects of Glauconite on Some Openhole Logs from the Lower Senonian in Egypt," in SPWLA 34th Annual Logging Symposium (Houston, TX, USA: Society of Petrophysicists and Well Log Analysts (SPWLA)).

Pham V. T. H., Halland E. K., Tappel I. M., Gjeldvik I. T., Riis F., and Aagaard P. (2013b). Long-term Behavior of CO2 Stored on a Large Scale in the Utsira Formation, the North Sea, Norwegian Continental Shelf. *Energ. Proced.* 37, 5240–5247. doi:10.1016/j.egypro.2013.06.440

Pham V. T. H., Riis F., Gjeldvik I. T., Halland E. K., Tappel I. M., and Aagaard P. (2013a). Assessment of CO2 Injection into the South Utsira-Skade Aquifer, the North Sea, Norway. *Energy* 55, 529–540. doi:10.1016/j.energy.2013.03.026

Ringrose P. S., Furre A. K., Gilfillan S. M. V., Krevor S., Landrø M., Leslie R., et al. (2021). Storage of Carbon Dioxide in Saline Aquifers: Physicochemical Processes, Key Constraints, and Scale-Up Potential. *Annu. Rev. Chem. Biomol. Eng.* 12, 471–494. doi:10.1146/annurev-chembioeng-093020-091447

Rundberg Y., and Eidvin T. (2005). Controls on Depositional History and Architecture of the Oligocene-Miocene Succession, Northern North Sea Basin. *Norwegian Pet. Soc. Spec. Publications* 12, 207–239. doi:10.1016/s0928-8937(05)80050-5

Rundberg Y., and Eidvin T. (2016). Discussion on 'Late Cenozoic Geological Evolution of the Northern North Sea: Development of a Miocene Unconformity Reshaped by Large-Scale Pleistocene Sand Intrusion'. *J. Geol. Soc.* 173, 384–393. doi:10.1144/jgs2014-023

Rundberg Y. (1989). *Tertiary Sedimentary History and Basin Evolution of the Norwegian North Sea between 60°-62°N: An Integrated Approach*. PhD thesis. Trondheim, (Norway): University of Trondheim.

Singh V., Cavanagh A., Hansen H., Nazarian B., Iding M., and Ringrose P. (2010). "Reservoir Modeling of CO2 Plume Behavior Calibrated against Monitoring Data from Sleipner, Norway," in SPE Annual Technical Conference and Exhibition (Florence, Italy, 19–22. doi:10.2118/134891-ms

Span R., and Wagner W. (1996). A New Equation of State for Carbon Dioxide Covering the Fluid Region from the Triple-Point Temperature to 1100 K at Pressures up to 800 MPa. *J. Phys. Chem. reference Data* 25, 1509–1596. doi:10.1063/1.555991

Stark C., and Thompson M. (2019). *Net Zero the UK's Contribution to Stopping Global Warming*. Climate Change Committee.

Stewart M. A., Lonergan L., and Hampson G. (2013). 3D Seismic Analysis of Buried Tunnel Valleys in the central North Sea: Morphology, Cross-Cutting Generations and Glacial History. *Quat. Sci. Rev.* 72, 1–17. doi:10.1016/j.quascirev.2013.03.016

Thibeau S., Nghiem L. X., and Ohkuma H. (2007). "A Modeling Study of the Role of Selected Minerals in Enhancing CO2 Mineralization during CO2 Aquifer Storage," in SPE Annual Technical Conference and Exhibition (USA: California), 11–14.

Thibeau S., and Mucha V. (2011). Have We Overestimated Saline Aquifer CO2Storage Capacities?. *Oil Gas Sci. Technol. - Rev. IFP Energies Nouvelles* 66, 81–92. doi:10.2516/ogst/2011004

Thibeau S., Seldon L., Masserano F., Canal Vila J., and Ringrose P. (2018). Revisiting the Utsira Saline Aquifer CO$_2$ Storage Resources Using the SRMS Classification Framework. *14th Greenhouse Gas Control. Tech. Conf. Melbourne* 1, 21–26. doi:10.2139/ssrn.3366195

Vangkilde-Pedersen T., Anthonsen K. L., Smith N., Kirk K., neele F., van der Meer B., et al. (2009). Assessing European Capacity for Geological Storage of Carbon Dioxide-The EU GeoCapacity Project. *Energ. Proced.* 1, 2663–2670. doi:10.1016/j.egypro.2009.02.034

Wrona T., Jackson C. A.-L., Huuse M., and Taylor K. G. (2017). Silica Diagenesis in Cenozoic Mudstones of the North Viking Graben: Physical Properties and basin Modelling. *Basin Res.* 29, 556–575. doi:10.1111/bre.12168

Wu L., Thorsen R., Ottesen S., Meneguolo R., Hartvedt K., Ringrose P., et al. (2021). Significance of Fault Seal in Assessing CO2 Storage Capacity and Containment Risks−An Example from the Horda Platform, Northern North Sea. *Pet. Geosci.* 27, 1. doi:10.1144/petgeo2020-102

Yang Y., and Aplin A. C. (2004). Definition and Practical Application of Mudstone Porosity-Effective Stress Relationships. *Pet. Geosci.* 10, 153−162. doi:10.1144/1354-079302-567

Ziegler P. A. (1990). *Geological Atlas of Western and central Europe*. Hague; Bath: Shell Internationale Petroleum; Distributed by Geological Society Publishing House.

Zweigel P., Arts R., Lothe A. E., and Lindeberg E. B. G. (2004). Reservoir Geology of the Utsira Formation at the First Industrial-Scale Underground CO2 Storage Site (Sleipner Area, North Sea). *Geol. Soc. Lond. Spec. Publications* 233, 165−180. doi:10.1144/gsl.sp.2004.233.01.11